Likelihood-Based Topological Reconstruction in JUNO

BACHELOR-THESIS

by Puja Leon Khanbaba-Tehrani

presented on: 25. September 2020

Univerity of Hamburg, research group neutrino physics

First appraiser: Dr. Björn Wonsak
Second appraiser: Prof. Dr. Caren Hagner

Abstract

JUNO, an acronym for Jiangmen Underground Neutrino Observatory, is a 20 kt liquid scintillator (LS) neutrino detector currently under construction in Jiangmen, China. With a planned energy resolution of 3% at 1 MeV, JUNO aims to answer the question of the ordering of the neutrino mass eigenstates and measure oscillation parameters with unprecedented precision. With the initial goal of reducing the background in large liquid scintillator detectors, the 3-D topological track reconstruction (TTR) was developed. It uses the time information of the scintillation light to reconstruct the original event topology, which it describes with a 3-D probability density function for the emission of scintillation light in the detector. This thesis deals with the implementation of the negative logarithmic likelihood (NLL) into the the TTR under JUNOs geometry. Applied to the TTR, the NLL compares the signature resulting from the reconstructed event topology with the detected event signature. The NLL hereby produces lower values the better and higher values the worse the signatures match up. Therefore, the NLL can be used as a measure of quality for the TTR results. The implementation of the method is approached by separating the combined-NLL $\mathscr{L}_{combined} = \mathscr{L}_{charge} + \mathscr{L}_{time}$ into two independent likelihoods describing the charge distribution, $\mathscr{L}_{charge}$, and the time distribution, $\mathscr{L}_{time}$ detected by the photomultiplier tubes (PMTs) of JUNO. A statistical analysis of the charge-NLL, using a toy-Monte-Carlo, with 10,000 simulated 3.5 MeV electron events, shows a resolution for the vertex reconstruction of low energy events (E < 5 MeV) of $\pm$ 28.2 cm for the X-direction, $\pm$ 28.0 cm for the Y-direction and $\pm$ 32.9 cm for the Z-direction. The time-NLL is tested by comparing its behaviour to the expected behaviour, with the results showing a correctly working method. Furthermore, an analysis, using a toy-Monte-Carlo, of a small sample of 100 events indicates a resolution for the vertex Reconstruction of low energy events of $\pm$ 20.3 cm for the X-direction, $\pm$ 21.1 cm for the Y-direction and $\pm$ 19.6 cm for the Z-direction. Application of the NLL on a well reconstructed event shows promising results, as the NLL is decreasing with each iteration, as expected, and additionally, the alternation between even and odd numbered PMTs, used in the TTR, is visible in course of the NLL. Application to an erroneous reconstruction shows a significant increase of the NLL in the final iteration, in which the artifact is most pronounced.

Zusammenfassung

JUNO, ein Akronym für Jiangmen Underground Neutrino Observatory, ist ein 20 kt Flüssigszintillator Neutrino Detektor in Jiangmen, China, der sich momentan im Bau befindet. Mit einer geplanten Energieauflösung von 3% bei 1 MeV zielt JUNO auf die Beantwortung der Frage nach der Massenordnung der Neutrino Masseneigenzustände und auf die Messung von Oszillationsparametern mit noch nie erreichter Präzision. Die 3-D topologische Spur Rekonstruktion (TTR) wurde mit dem initialen Ziel den Hintergrund in großen Flüssigszintillator Detektoren zu reduzieren, entwickelt. Sie benutzt die Zeitinformationen des Szintillationslichtes um die ursprüngliche Ereignistopologie zu rekonstruieren, welche sie durch eine 3-D Wahrscheinlichkeitsdichtefunktion der Emissionswahrscheinlichkeit von Szintillationslicht im Detektor beschreibt. Diese Bachelorarbeit beschäftigt sich mit der Implementierung der negative logarithmic likelihood (NLL) in die TTR unter JUNOs Geometrie. Angewendet auf die TTR vergleicht die NLL die Signatur, die durch die rekonstruierte Ereignistopologie entsteht, mit der detektierten Ereignissignatur. Die NLL produziert hierbei umso niedrigere Werte, desto besser und umso höhere Werte, desto schlechter die Signaturen zueinander passen. Somit kann die NLL als Qualitätsmaß der Ergebnisse der TTR benutzt werden. Die Implementierung der Methode wird durch das Aufteilen der kombinierten-NLL $\mathscr{L}_{combined} = \mathscr{L}_{charge} + \mathscr{L}_{time}$ in zwei unabhängige likelihoods angegangen, welche die Ladungsverteilung, $\mathscr{L}_{charge}$, und die Zeitverteilung, $\mathscr{L}_{time}$, die von den Photomultiplier tubes (PMTs) von JUNO gemessen werden, beschreiben. Eine statistische Analyse der Ladungs-NLL, unter Benutzung einer toy-Monte-Carlo, mit 10,000 simulierten 3.5 MeV Elektronen Ereignissen zeigt eine Auflösung der Vertexrekonstruktion von niederenergetischen Events (E < 5 MeV) von $\pm$ 28.2 cm in X-Richtung, $\pm$ 28.0 cm in Y-Richtung und $\pm$ 32.9 cm in Z-Richtung. Die Zeit-NLL wird durch den Vergleich von ihrem Verhalten zu dem erwarteten Verhalten getestet, wobei die Ergebnisse eine funktionierende Methode zeigen. Zusätzlich deutet eine Analyse, unter Benutzung einer toy-Monte-Varlo, einer kleinen Stichprobe von 100 Ereignissen auf eine Auflösung bei der Vertexkonstruktion niederenergetischer Ereignisse von $\pm$ 20.3 cm in X-Richtung, $\pm$ 21.1 cm in Y-Richtung und $\pm$ 19.6 cm in Z-Richtung hin. Die Anwendung der NLL auf ein gut rekonstruiertes Event zeigt vielversprechende Resultate, da die NLL mit jeder Iteration sinkt, wie erwartet, und zusätzlich die Alternierung zwischen gerade und ungerade nummerierten PMTs, die in der TTR stattfindet, im Verlauf NLL erkennbar ist. Anwendung auf eine fehlerhafte Rekonstruktion zeigt einen signifikanten Anstieg der NLL in der letzten Iteration, in der das Artefakt am stärksten ausgeprägt ist.

Contents

Chapter 1

Introduction

Neutrino physics has gathered a lot of interest in the recent years. Beside the possibility of studying weak interactions, the discovery of neutrino oscillations opened an interesting field of study for physics beyond the Standard Model. Additionally, neutrinos provide the possibility of studying many other objects and phenomenons including solar models, supernovae and the inner earth. In the current state of understanding, multiple big questions about neutrinos remain unanswered, namely the ordering of the neutrino mass eigenstates, if neutrinos are their own anti particles and the possibility of CP-violation. To investigate neutrinos, determine the parameters of interest and answer the open questions, different detector types have been deployed. Of those, large liquid scintillator detectors have exceeded old expectations of their directional resolution and proven an effective and popular way to study neutrino behaviour. Detectors like KamLAND [1] and Double-Chooz [2] have contributed greatly to the current understanding of neutrino physics and the limit of liquid scintillator detectors is yet to be reached. With the Jiangmen Underground Neutrino Observatory (JUNO) detector, a 20 kt liquid scintillator detector, currently under construction in Jiangmen, China, a new milestone in energy resolution of 3% at 1 MeV is aimed for to answer the question of the ordering of the neutrino mass eigenstates. JUNO is strategically placed at a distance of 53 km to two nuclear power plants, which act as sources of reactor electron antineutrinos. Being the main signal of JUNO, the electron antineutrinos are detected via the inverse beta decay, occurring when an electron antineutrino interacts with a proton. Precise measurements of the energy spectrum of these reactor antineutrinos allow the determination of the mass ordering. Even with their enormous size, neutrino detectors usually have to measure over a period of multiple years to acquire a sufficient amount of data, due to the small cross-section of neutrino interactions. Vetoing detector space to reduce background is therefore costly and efforts are made to minimize the vetoed volume and the veto duration. JUNO will mostly struggle with cosmogenic Li^9 and He^8, produced by transiting muons, which can mimic the inverse beta decay signal in their decay. These cosmogenics are long lived and hard to locate. resulting in large volumes around the

path of tracked muons to be vetoed for several seconds to counteract the false signals.
In this thesis, a possible improvement to the 3-D topological track reconstruction (TTR) is introduced. The TTR is a method developed to analyse data from large-volume liquid scintillator experiments, with the original purpose of reconstructing hadronic showers along muon tracks to reduce the required vetoes. By using the information provided by the hit times and hit charges on each light detector, the topology of the event is reconstructed. Its application on JUNO is currently developed. The original goal of the TTR has been expanded, as it shows potential for many different applications, including vertex reconstruction and particle discrimination. Implemented in this thesis, the negative logarithmic likelihood (NLL) is tested as a means of monitoring the quality of the TTR, with the future goal of improving the reconstruction by adjusting it, based on minimizing the NLL. Using the NLL, the event signature can be compared to the signature resulting from the reconstructed event topology from the TTR, giving a quantitative measure for the quality of the reconstruction. Additionally, the NLL can be used as a criterion of termination of the iterative process of the TTR, which it is currently missing, and help prevent or notice artifacts and overfitting. Furthermore, the NLL holds potential for improving vertex reconstructions of low energy events.
The first chapter of this thesis will give an overview of the basics of neutrino physics, consisting of a brief introduction to the Standard Model, followed by a short explanation of the history of neutrinos and their characteristics. The overview is concluded by introducing the phenomenon of neutrino oscillations and its consequences. Afterwards the concept of liquid scintillator detectors will be explained, including a section going into more detail about photomultiplier tubes, which are commonly used in LS detectors. As the relevant LS detector of this thesis, JUNO will be introduced and explained, addressing not only its design but also its physics goals, main signal and backgrounds for that main signal. Subsequently, the TTR is explained, establishing the basis for the work of this thesis. Being the key component of this bachelor thesis, a short section is dedicated to define the NLL and clarify its functionality. Following the definition, the implementation of the NLL into the TTR is motivated, touching on immediate and future benefits it can provide. Next, the presentation of the results is separated into the charge-NLL, describing the charge distribution detected by the PMTs, and the time-NLL, describing the hit time distribution detected by the PMTs. Furthermore, a method of testing the implemented NLL using a toy-Monte-Carlo simulation is presented before the results of the application of the method to the TTR-results are shown. Finally, the results are interpreted in the conclusion, in which the successes and shortcomings of this thesis are discussed.

Chapter 2

Neutrino physics

2.1 Standard Model of particle physics

The Standard Model of particle physics is the umbrella term for current theoretical descriptions of all known elementary particles and three of the four fundamental forces. Being an umbrella term, its constituents were added over multiple decades and are meant to combine into a consistent description of the fundamental physics of particles and their interactions. In spite of the impressive record of experimentally verified predictions, the Standard Model fails to explain multiple important phenomena. Attempts to integrate gravity, the fourth fundamental force, into the Standard Model have not been successful and findings over the last few years, like the detection of neutrino oscillations, have repeatedly indicated that there is physics beyond the Standard Model. The Standard Model categorizes the fundamental particles into three groups: Twelve Fermions, which are further separated into quarks and leptons as well as thirteen Gauge bosons. Quarks and leptons each are further divided into three, so-called, families. These three quark families contain a pair of two quarks each, while the three lepton families each contain a pair of leptons. Lepton families consist of a charged lepton (e, μ, τ) and a neutral neutrino (ν_e, ν_μ, ν_τ), while the quark families contain two quarks with different fractional charge each (up/down, charm/strange, top/bottom). This categorization is visualized in Figure 2.1. For each quark (lepton) there is an antiquark (antilepton) which has almost the same characteristics as its counterpart, but for non-neutral particles, the antiparticle has the opposite charge. For the neutral neutrinos, the nature of their antiparticles is still in question, as it is uncertain if they are Majorana particles, meaning that they are their own antiparticles.

Within the Standard Model, forces are described via the exchange of virtual particles. Therefore, each force has one or multiple exchange particles, the gauge bosons, associated with it. As mentioned above, the Standard Model includes three fundamental forces: electromagnetism, the strong force and the weak force with their gauge bosons the photon, the gluons and the $W^{\pm}$ and Z^0 bosons, respectively. The electro-

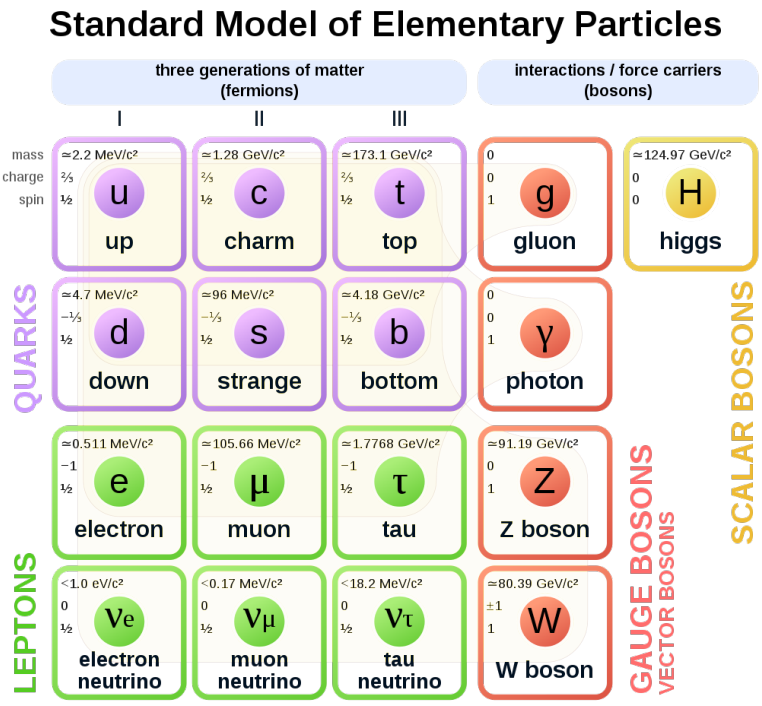

Figure 2.1: Overview of the particles of the Standard Model of particle physics. Neutrino mass limits, which are not part of the Standard Model, are included [3].

magnetic force is transmitted via the neutral and massless photon, with an unlimited range. The strong interaction is propagated by eight gluons ($r\bar{g}$, $r\bar{b}$, $g\bar{b}$, $g\bar{r}$, $b\bar{r}$, $b\bar{g}$, $\frac{1}{\sqrt{2}}(r\bar{r}-g\bar{g})$ $\frac{1}{\sqrt{6}}(r\bar{r}+g\bar{g}-2b\bar{b})$), which carry the so called color charges (c), composed of red (r), green (g) and blue (b) with their respective anti-charges ($\bar{c}$) antired ($\bar{r}$), antigreen ($\bar{g}$) and antiblue ($\bar{b}$) . Despite gluons being massless, the range of the strong interaction is very short ($\approx 10^{-15}$ m) and rapidly increasing in strength with distance due to gluon-gluon interactions, as they carry color charge themselves. Quarks can not be found as free particles because of the short range of the strong force. Instead color neutral ($c\bar{c}$, *rgb or* $\bar{r}\bar{g}\bar{b}$) hadrons form, which are particles composed of quarks.
Weak charge is carried by every fundamental fermion, making the weak force the only force to change the flavour of quarks and interact with the otherwise neutral neutrinos. It is exchanged through the massive $W^{\pm}$ and Z^0 bosons. Its range ($\approx 10^{-18}$ m) and, for low particle energies, coupling strength are small due to the high mass of its gauge bosons ($M_{W^{\pm}} \approx 80.379 \pm 0.012 \frac{\text{GeV}}{c^2}$ and $M_Z^0 \approx 91.1876 \pm 0.0021 \frac{\text{GeV}}{c^2}$ [4]) [5]. A prominent example for the change of quark flavor is the β^- decay, in which a neutron decays into a proton, an electron and an anti-electron neutrino

$$n \rightarrow p + e^- + \bar{\nu}_e. \tag{2.1}$$

Looking at the β^- decay on quark level, a down quark of the neutron weakly decays via a W^- boson, changing flavor to an up quark, and the W^- boson decays into an electron

and an electron antineutrino, visualized in Figure 2.2.

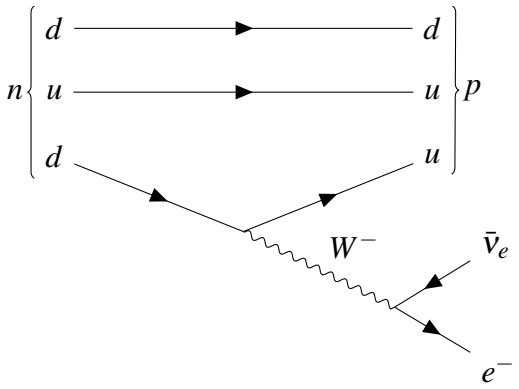

Figure 2.2: Feynman diagram of the β^- decay on quark level. A down (d) quark of the neutron (n) weakly decays via a W^- boson, changing flavour to an up quark (u), and the W^- decays into an electron (e^-) and and an electron antineutrino ($\bar{\nu}_e$).

2.2 Neutrinos

Neutrinos have been postulated in 1930 by Wolfgang Pauli, to explain the observed continuous energy spectrum of the electron in a β^- decay (Equation 2.1). Without the neutrino, the β^- decay would be a three particle interaction,

$$n \rightarrow p + e^-, \tag{2.2}$$

and the decay in a nucleus would lead to discrete kinetic energies of the electron. Proposing a third particle, here the neutrino, which escapes detection would solve this discrepancy, as the neutrino could carry any fraction of the overall kinetic energy, resulting in the observed continuous electron energy spectrum. The discovery of the Neutrino occured in 1956 by Reines and Cowan, by detecting the inverse beta decay (IBD) (Equation 2.3) [6]. More detail on the experiment is given later in this section.
There are three flavours of neutrinos (antineutrinos), each grouped in a family with one of the charged leptons (antileptons). In the Standard Model, neutrinos are assumed to be massless, which was proven wrong by the observation of neutrino oscillations, a phenomenon requiring massive neutrinos. So far the masses could not be measured but an upper limit, valid for all three flavours, has been established to $m_\nu \leq 1.1 \ \frac{eV}{c^2}$ [7]. To set this limit, the KATRIN experiment made high precision measurements near the maximum of the electron energy spectrum of the beta decay (Equation 2.1) of tritium. The electron and electron antineutrino emitted by this decay have a combined energy of 18.6 keV distributed between the rest mass of the antineutrino and the kinetic energy of the electron and antineutrino. By precisely measuring the electron energy spectrum close to the maximum energy, an upper limit for the neutrino mass can be determined,

as the maximum kinetic energy of the electron is limited by the rest mass of the antineutrino [8].

Neutrinos are produced by many different sources and neutrinos used in experiments are usually named based on their source. The most prominent neutrino sources include the sun (solar neutrinos), cosmic radiation (cosmic neutrinos), atmospheric showers produced by cosmic radiation (atmospheric neutrinos) and nuclear reactors (reactor neutrinos). Some experiments are also performed on high intensity neutrino beams produced by particle accelerators. As neutrinos only interact weakly, reaction cross sections are small and direct detection is technically not possible. Instead, detectors, shielded from unwanted radiation, detect particles resulting from neutrinos interacting within a large target mass. An example for neutrino detection is the initial discovery of neutrinos by Reines and Cowan, mentioned above, using reactor neutrinos. The experiment consisted of a container filled with cadmium chloride solved in water, which was placed in between two liquid scintillators (explained in chapter 3) equipped with photomultipliers (explained in section 3.1) to detect the emitted photons. The idea was, that a reactor antineutrino interacts with a proton within the container, resulting in the inverse beta decay

$$\bar{\nu}_e + p \rightarrow e^+ + n \tag{2.3}$$

and producing a positron and a neutron in the process. The positron quickly annihilates with an electron

$$e^+ + e^- \rightarrow \gamma + \gamma, \tag{2.4}$$

producing two gammas with $E_\gamma = m_e = 0.511$ MeV each, which are detected by the scintillation counters. The neutron slows down over the course of a few microseconds before being caught by a cadmium core, leading to the emission of gammas by the cadmium due to relaxation processes. This leads to a unique, characteristic signature of the monochromatic gamma pair followed by a delayed signal of the relaxation gammas, which allowed Reines and Cowan to prove the existence of neutrinos and measure the cross section for the observed inverse beta decay. [6]

2.3 Neutrino oscillations

Neutrino oscillation labels the phenomenon of neutrino flavour-transitions. They are described by the PMNS (Pontecorvo-Maki-Nakagawa-Sakata) matrix U, expressing the flavour eigenstates $\nu_{e,\mu,\tau}$ as a linear combination of three mass eigenstates $\nu_{1,2,3}$ (Equation 2.5), whereby the flavour eigenstates are the observables:

$$\begin{pmatrix} |\nu_e\rangle \\ |\nu_\mu\rangle \\ |\nu_\tau\rangle \end{pmatrix} = \begin{pmatrix} U_{e1} & U_{e2} & U_{e3} \\ U_{\mu 1} & U_{\mu 2} & U_{\mu 2} \\ U_{\tau 1} & U_{\tau 2} & U_{\tau 3} \end{pmatrix} \cdot \begin{pmatrix} |\nu_1\rangle \\ |\nu_2\rangle \\ |\nu_3\rangle \end{pmatrix}. \tag{2.5}$$

Following the structure of [5] and [9], a simplified case of only two flavour and mass states (Equation 2.6) can be used to explain the matrix and its implications. For this the mixing angle θ is introduced:

$$\begin{pmatrix} |\nu_e\rangle \\ |\nu_\mu\rangle \end{pmatrix} = \begin{pmatrix} \cos\theta & \sin\theta \\ -\sin\theta & \cos\theta \end{pmatrix} \cdot \begin{pmatrix} |\nu_1\rangle \\ |\nu_2\rangle \end{pmatrix}. \tag{2.6}$$

With this Matrix (Equation 2.6) the electron neutrino flavour state can therefore be written as

$$|\nu_e\rangle = \cos(\theta)\,|\nu_1\rangle + \sin(\theta)\,|\nu_2\rangle \tag{2.7}$$

and its time development as

$$|\nu_e(t)\rangle = \cos(\theta)\,e^{-iE_{\nu_1}t/\hbar}\,|\nu_1\rangle + \sin(\theta)\,e^{-iE_{\nu_2}t/\hbar}\,|\nu_2\rangle, \tag{2.8}$$

where t is the time and $\hbar$ is the reduced Planck constant. Being ultra-relativistic, the energy of the neutrino E_{ν_i} can be approximated to

$$E_{\nu i} = \sqrt{p^2c^2 + m_{\nu i}^2c^4} \approx pc\left(1 + \frac{1}{2}\frac{m_{\nu i}^2c^4}{p^2c^2}\right), \tag{2.9}$$

where p is the momentum of the neutrino, c is the speed of light in a vacuum and m_{ν_i} is the mass of the neutrino ν_i. Finally, we can calculate the probability for the transition electron neutrino to electron neutrino ($\nu_e \to \nu_e$) after a time t:

$$P_{\nu_e\to\nu_e} = \left|\langle\nu_e(t)|\nu_e\rangle\right|^2 = 1 - \sin^2(2\theta)\sin^2\left(\frac{1}{4}\frac{\Delta m_{21}^2c^4}{\hbar c}\frac{L}{E}\right). \tag{2.10}$$

Where

$$\Delta m_{21}^2 = m_{\nu 2}^2 - m_{\nu 1}^2 \tag{2.11}$$

is the difference of the square of the masses (in the following simply referred to as mass difference) of the mass eigenstates $\nu_{1,2}$ and $L = ct$ is the distance covered in time t, between the creation of the neutrino and the measurement and $E = pc$ is the kinetic energy of the neutrino. This means that the transition probability oscillates with a frequency depending on $\frac{L}{E}$. The mixing angle defines the amplitude, while the mass difference defines the frequency of the oscillation. From this the probability for the transition electron neutrino to muon neutrino ($\nu_e \to \nu_\mu$) follows as

$$P_{\nu_e\to\nu_\mu} = 1 - P_{\nu_e\to\nu_e} = \sin^2(2\theta)\sin^2\left(\frac{1}{4}\frac{\Delta m_{21}^2c^4}{\hbar c}\frac{L}{pc}\right). \tag{2.12}$$

The PMNS matrix can also be parametrized with mixing angles. In addition, it contains

a phase angle δ_{CP} for the possibility of charge-parity violations.

$$U = \begin{pmatrix} c_{12}c_{13} & s_{12}c_{13} & s_{13}e^{-i\delta_{CP}} \\ -s_{23}c_{23} - c_{12}s_{23}s_{13}e^{i\delta_{CP}} & c_{12}c_{23} - s_{12}s_{23}s_{13}e^{i\delta_{CP}} & s_{23}c_{13} \\ s_{12}s_{23} - c_{12}c_{23}s_{13}e^{i\delta_{CP}} & -c_{12}s_{23} - s_{12}c_{23}s_{13}e^{i\delta_{CP}} & c_{23}c_{13} \end{pmatrix}, \quad (2.13)$$

where $c_{ij} = \cos\theta_{ij}$, $s_{ij} = \sin\theta_{ij}$, i,j = 1,2,3. To further account for the possibility of Majorana neutrinos, two free ρ and ϕ parameters are introduced:

$$U_M = U \cdot \begin{pmatrix} 1 & 0 & 0 \\ 0 & e^{i\rho} & 0 \\ 0 & 0 & e^{i\phi} \end{pmatrix}. \quad (2.14)$$

The CP-phase δ_{CP}, as well as the free parameters for Majorana neutrinos are not to be expanded upon here. The three flavour case, though more complex, is analogous to the two flavour case. The flavour states $\nu_{e,\mu,\tau}$ can be written as a superposition of the mass eigenstates $\nu_{1,2,3}$. The time development of a neutrino with flavour ν_α, emitted at $t = 0$, can be written as

$$\left|\nu(x,t)\right\rangle = \sum_i U_{\alpha,i} e^{-iE_i t} \left|\nu_i\right\rangle = \sum_{i,\beta} U_{\alpha,i} U^*_{\beta,i} e^{ipx} e^{-iE_i t}, \quad (2.15)$$

where α and β represent flavours and i represents mass eigenstates with E_i being the energy of that eigenstate [9]. The probability for a flavour transition $\nu_\alpha \to \nu_\beta$ can then be written as

$$\begin{aligned} P(\alpha \to \beta)(t) &= \left|\left\langle \nu_\beta \middle| \nu(x,t) \right\rangle\right|^2 = \sum_i \sum_j U_{\alpha,i} U^*_{\alpha,j} U^*_{\beta,i} U_{\beta,j} e^{-i(E_i - E_j)t} \\ &= \sum_i \left|U_{\alpha,i} U^*_{\beta,i}\right|^2 + Re\left(\sum_{j>i} U_{\alpha,i} U^*_{\alpha,j} U^*_{\beta,i} U_{\beta,j} \exp(-i\frac{\Delta m^2_{ij}}{2})\frac{L}{E}\right), \end{aligned} \quad (2.16)$$

with the distance to the source L, the energy of the neutrino E and the squared mass difference Δm^2.

With this, it is possible to determine the elements of U, as well as the difference of the squared masses of the mass eigenstates by measuring the probability of survival or the appearance of the different flavours. For this purpose, detectors can be build at specific distances L from nuclear reactors or neutrino beams to maximize sensitivity and test predictions made by this model.

Multiple mixing angles as well as mass differences have been measured at varying precision. While the value of mass differences has been determined, only the sign of Δm^2_{21} is known. This results in the current question of ordering of the mass eigenstates, which is either the normal ordering or the inverted ordering, depending on the sign of Δm^2_{32}. The normal and inverted oderings are visualized in Figure 2.3, showing the squared

mass eigenstates m_1^2, m_2^2, m_3^2 and their relative composition, if written as a superposition of the flavor eigenstates ν_e, ν_μ, ν_τ. Knowing the mass ordering is important for further understanding of neutrinos, as, e.g., the measurement of the CP-violating phase δ is dependant on the correct ordering [10].

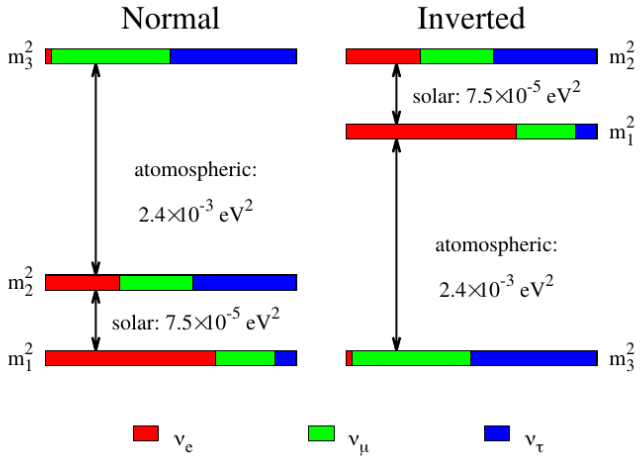

Figure 2.3: Visualization of the normal ordering (left) and the inverted ordering (right) of the neutrino masses [11].

Chapter 3

Liquid scintillator detectors

Conceptually, liquid scintillator detectors use a large volume of liquid scintillator as their target mass, which is surrounded by light detectors (commonly PMTs) to capture the scintillation light, which is produced when energy is deposited by transiting ionizing particles. An ionizing particle produced within or traveling through the detector volume excites scintillator molecules along its path, resulting in the emission of scintillation light. To be detected, this scintillation light has to travel from its point of emission to one of the PMTs of the detector. On its way, the light can be completely absorbed, absorbed and re-emitted or scattered, loosing or smearing all or parts of its initial temporal and spatial information of the event. For this, the attenuation length of the light in the fluid is important. The attenuation length L defines the penetration depth x of a material, at which the probability of a particle not being absorbed or scattered has dropped to $\frac{1}{e}$:

$$P(x) = e^{\frac{-x}{L}} \tag{3.1}$$

Since the attenuation length is dependant on the wavelength of the photons, wavelength-shifters are added to the liquid scintillator to increase the attenuation length, decreasing absorption and scattering and therefore increasing the yield of detected photons. Since the scintillator is resonant at the emitted wavelengths and would therefore reabsorb the emitted light, wavelenght-shifters are a necessary component. Energy transfer between the scintillator and the wavelength-shifter can happen through non-radiant transitions, further reducing the potential for reabsorbtion of scintillation light. Furthermore, the addition of wavelength-shifters can be used to shift the scintillation light, which is usually at a wavelength in the region around ultraviolet, to a wavelength, at which the used light detectors are sensitive. Scintillation light is emitted isotropically and therefore does not carry any directional information.
The time spectrum of the scintillation light can be approximated by a weighted sum of

exponential function with different decay parameters:

$$F_{scint}(t,\tau,\omega) = \sum_{i=1}^{n} \frac{\omega_i}{\tau_i} \cdot e^{-\frac{t-t_0}{\tau_i}}, \tag{3.2}$$

where t is the time, τ_i are different decay time constants and ω_i are weights that sum up to 1 [12].

While scintillation light makes up over 90 % of the light yield of liquid scintillator detectors, the particles passing through also produce Cherenkov radiation. Cherenkov light is the optical equivalent of a sonic boom and is produced whenever a charged particle transits a medium at a speed that exceeds that medium's speed of light. The speed of a photon is dependant on its wavelength λ and the refractive index n of the medium given by

$$v_{\text{phase}} = \frac{c}{n(\lambda)}. \tag{3.3}$$

The charged particle polarizes the molecules along its path, which promptly emit photons as they relax. As visualized in Figure 3.1, the particle induced the emission of radial waves, which propagate slower than the source-particle, resulting in a shock front of light. The angle of the cone is given by

$$cos(\theta) = \frac{1}{n(\lambda)\beta}, \tag{3.4}$$

where β is the relativistic factor defined by the particle velocity v_{particle} and c

$$\beta = \frac{v_{\text{particle}}}{c}. \tag{3.5}$$

Cherenkov light therefore contains directional information of the particle of interest. In LS detectors this potential directional information is difficult to use, as the proportion of Cherenkov light is very small. In contrast to the scintillation light, Cherenkov light is promptly emitted. This distinction could aid in seperating Cherenkov and scintillation light during data analysis. Utilizing Cherenkov light in the analysis of LS detector data is subject of current research and could become a relevant part of the data analysis in LS detectors in the future.

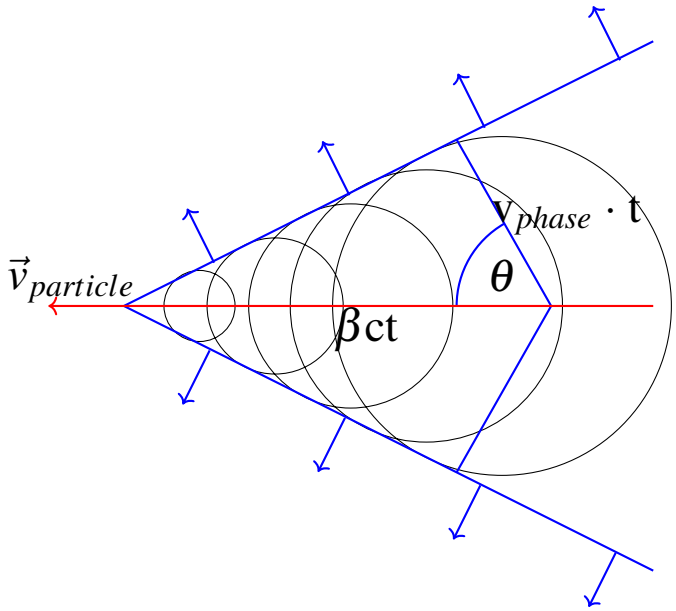

Figure 3.1: Illustration of idealised Cherenkov radiation.

3.1 Photomultiplier Tubes

A photomultiplier tube (PMT) is a sensitive electronic setup for the detection of photons, capable of resolving singular photons. The general design includes a photocadode, working as the light sensitive trigger, followed by a multiplying mechanism to amplify the final signal reaching the anode, where it is registered as a drop in voltage. This setup is usually contained in a vacuous glass tube or bulb. The basic idea is the emission of a photoelectron by the photocatode when hit by a photon, which triggers the multiplying mechanism. The multiplying mechanism drastically increases the number of electrons that hit the anode, resulting in a measurable voltage drop. The amplification is usually around a factor of $10^6 - 10^7$.

For the purpose of this thesis, two types of PMTs are of interest:

Dynode PMTs, schematic illustration in Figure 3.2, use a series of electrodes, called dynodes, as a multiplying meachnism. Measurements begin with a photon hitting the photocathode of the PMT, resulting in the emission of an electron according to the photoelectric effect. The photoelectron is accelerated onto a dynode by an acceleration voltage, where it produces multiple secondary electrons. The secondary electrons are then accelerated onto another dynode. This process is repeated around 10 times before the resulting electron avalanche hits the anode.

Microchannel plates (MCPs), schematic illustration in Figure 3.3, use a semiconducting material, which is perforated at a slight angle, resulting in a number of tunnels, only a few micrometer in diameter, reaching from one end to the other. This block is positioned between a photocathode and an anode. The photoelectron enters a tunnel of the MCP and hits the slightly angled wall, producing secondary electrons. Repeating this

throughout the length of the holes results in the mentioned electron avalanche.

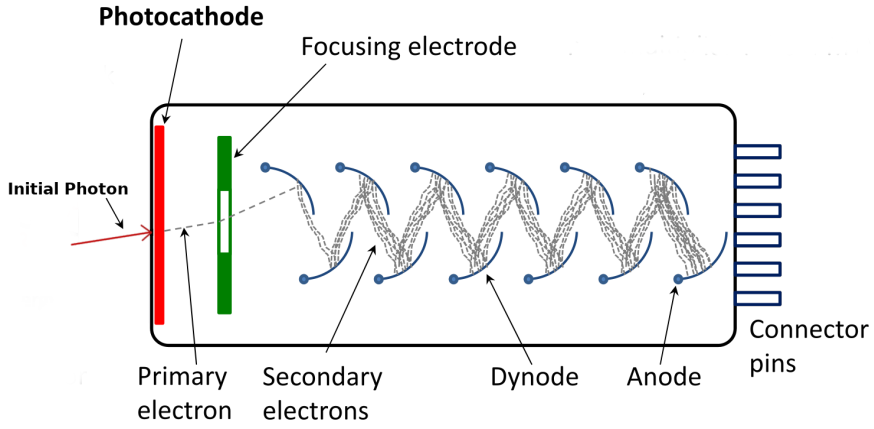

Figure 3.2: Schematic representation of a dynode PMT. (Edited [13])

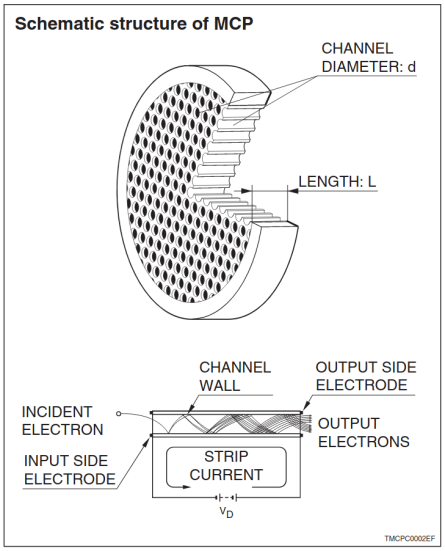

Figure 3.3: Schematic representation of a MCP PMT. [14]

When working with PMTs it is important to know sources of errors and their significance. For example, making up a predictable part of the noise, the dark count rate is the count rate of a PMT in the absence of light, mostly having its origin in thermal effects. The transit time spread (TTS) defines the inaccuracy of the detection of the time of a hit. The main factor is the extended photocathode, which results in slightly different travel times for the photoelectrons, based on the position of the photon hit. The TTS is described as a Gaussian smearing all measured hit times, with its width depending on the PMT in question. Given by the ratio of photons N hitting the PMT and the number of photons detected N_{det} by the PMT the photo detection efficiency (PDE),

$$PDE = \frac{N_{det}}{N}, \tag{3.6}$$

gives a measure for the amount of photons detected out of all photons that hit the PMT,

constituting an important factor in reconstructing a detected event. Exemplary values for these factors can be found in Table 3.1.

3.2 JUNO

JUNO, an acronym for Jiangmen Underground Neutrino Observatory, is a liquid scintillator based neutrino observatory currently under construction in Jiangmen, China. It is located 700 meters underground at a distance of 53 kilometers to the Yangjiang and the Taishan nuclear power plant [11], which are acting as sources of reactor neutrinos.

Detector layout

The detector layout, here described from inside to outside, begins with the central detector. The target mass, about 20 kilotons of a mixture of liquid scintillator and wavelength-shifter, fills a 35.4 meter diameter acrylic sphere. This acrylic sphere is supported by a surrounding stainless-steel scaffolding with a diameter of 40 meters. On the scaffolding, $\sim$18,000 20" PMTs and $\sim$25,000 3.1" PMTs are installed, achieving a coverage of $\sim$77 %. They are separated from the inner sphere by 1.7 meters. The TTS, dark count rates and PDE of the PMTs used in JUNO are summarized in Table 3.1. This setup is submerged in a cylindrical pool of ultra pure water, acting as a radiation shield. Additionally, the pool is outfitted with $\sim$1500 20" PMTs, making it a water Cherenkov detector able to veto muons entering the central detector volume from the outside [15] [16] [11]. On top of the cylindrical water volume a, top tracker, consisiting of six layers of plastic scintillator, is installed to gather additional information on muon tracks.

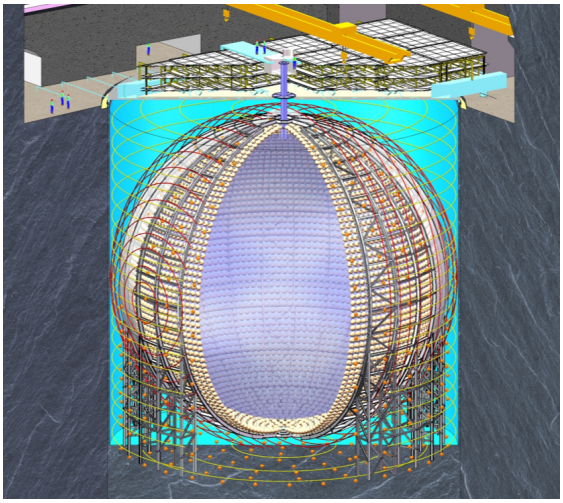

Figure 3.4: Schematic view of the JUNO Detector [17].

JUNO will use a liquid scintillator based on linear alkyl benzene (LAB) mixed with

a two-component Fluor (PPO) and an additional wavelength-shifter (Bis-MSB) [15]. After being wavelength-shifted, the light will be at a wavelength of around 430 nm, at which the PMTs are especially sensitive and the attenuation length will be over 22 meters. JUNO aims to achieve an energy resolution of 3% at 1 MeV, with about 12,000 emitted scintillation photons/MeV while measuring at least 1200 photoelectrons per MeV of deposited energy [15]. In JUNO, Cherenkov radiation will make up only around 3% of the light yield, having little impact on the analysis of scintillation light.

Table 3.1: Summary of important PMT-properties [10].

Type	Hamamatsu R12860 HQE	NNVT model	HZC XP72B22
quantity	~5,000	~13,000	~25,000
size	20 inch	20 inch	3.1 inch
multiplier	dynode	MCP	dynode
PDE at λ_{photon} =420 nm	24 % - 35 %	24 % - 35 %	22 % - 27 %
TTS (FWHM)	3 ns	20 ns	4.5 ns
Darkcountrate	< 50 kHz	< 100 kHz	< 1.8 kHz

Physics program

The main goal of JUNO is to answer the question of the neutrino mass ordering, which is explained at the end of section 2.3. Additionally, Δm^2_{21} and $\sin^2(\theta_{12})$ are to be measured with unprecedented precision. To give an overview, Table 3.2 summarizes the current measurements of the parameters of interest, including the targeted precision of JUNO.

Table 3.2: Best fit values, as well as 1σ range in percent and the expected sensitivity of JUNO for the oscillation parameters of interest [11] [18].

Parameter	Best fit	1σ range	JUNO
$\Delta m^2_{21}/10^{-5}\ eV^2$	7.39	$\approx$ 2.8 %	< 1 %
$\sin^2\theta_{12}$	0.310	$\approx$ 4.2 %	< 1 %

Additionally, JUNO provides the potential to study atmospheric neutrinos, geo neutrinos and supernova neutrinos [19].

JUNOs main signal is the inverse beta decay (Equation 2.3), where a reactor electron-antineutrino reacts with a proton of the target mass. That means JUNO uses the same coincidental signature of the prompt positron annihilation into two gammas and the delayed neutron energy deposit as Reines and Cowan utilized in their discovery of the neutrino (explained in section 2.2). The positron carries the majority of the energy of the antineutrino, enabling the measurement of the antineutrino spectrum via the prompt signal, as the positron produces scintillation light before annihilating [11]. Figure 3.5 shows the probability of survival for electron antineutrinos $P(\bar{\nu}_e \rightarrow \bar{\nu}e)$ at different *L/E*

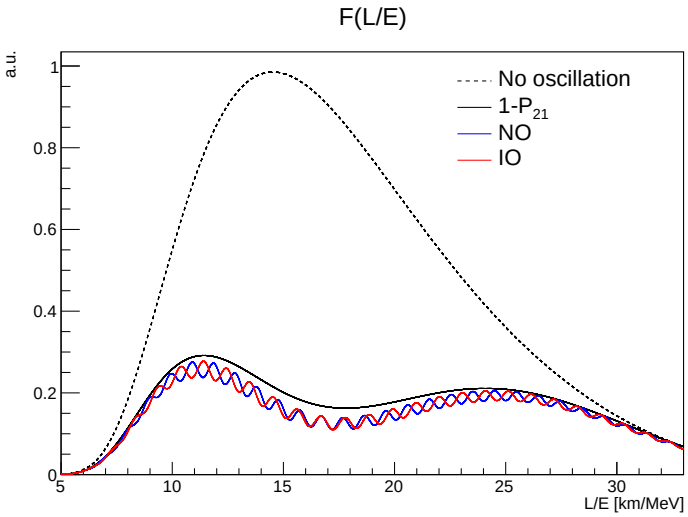

Figure 3.5: Representation of the relative quantity of surviving electron antineutrinos at different *L/E*. To be published in [20].

according to

$$P(\bar{\nu}_e \to \bar{\nu}_e) = 1 - \sin^2(2\theta_{12}) \cdot c_{13}^4 \cdot \sin^2\left(\frac{\Delta m_{21}^2 L}{4E}\right) - \sin^2(2\theta_{13}) \cdot \left[c_{12}^2 \cdot \sin^2\left(\frac{\Delta m_{31}^2 L}{4E}\right) + s_{12}^2 \cdot \sin^2\left(\frac{\Delta m_{32}^2 L}{4E}\right)\right], \tag{3.7}$$

using the same definitions as introduced in section 2.3. Its basis is the electron antineutrino spectrum JUNO will see based on the reactor flux and the reaction cross-section, visualized by the dotted line, which shows the predicted spectrum without the phenomenon of neutrino oscillations. The solid black line shows the development according to the transition probability given by only the first and second term, $1 - \sin^2(2\theta_{12}) \cdot c_{13}^4 \cdot \sin^2(\frac{\Delta m_{21}^2 L}{4E})$, in Equation 3.7. Recognizable as a finer oscillation structure imprinted on the general form of the oscillation, the difference between the normal ordering and the inverted ordering is overlayed as a solid blue and red line, respectively. This finer oscillation is due to the third term in Equation 3.7, which includes Δm_{31}^2. A precise measurement of the neutrino spectrum can therefore be subject to a spectral analysis in order to answer the question of mass ordering. The mentioned energy resolution of 3 % at 1 MeV is essential for this process. The more in-depth and complex calculations regarding the determination of the mass ordering from the energy spectrum can be found in [11]. It is predicted that JUNO has to measure for about 6 years to achieve the determination of the mass ordering and the targeted precision.
In JUNO, five main sources of background obscure the main signal [11]:

- **Accidental**: The accidental background is composed two uncorrelated signals occurring in a short time frame at any distance to each other, mimicking the signal of an inverse beta decay.

- **^{9}Li/^{8}He**: Cosmogenic isotopes, commonly referred to as cosmogenics, are atomic isotopes, expelled from atoms in interaction with high-energy cosmic rays. In JUON, cosmogenic ^{9}Li and ^{8}He is produced, which can decay in a β-n decay, mimicking the main signal.

- **Fast neutrons**: Untagged muons can produce energetic neutrons by interacting with atoms in the detector. These neutrons can then scatter off a proton producing a recoil proton, which can be detected as a prompt signal. Either an independent or the inducing neutron can then be detected, resulting in a signal mimicking the inverse beta decay signal [21].

- **^{13}C + α $\rightarrow$^{16}O* + n**: Alpha particles from detector components can react with the ^{13}C in the LS, producing a neutron and leaving an excited ^{16}O. If this reaction produces a fast neutron or if the ^{16}O* deexcites under the emission of a gamma, the produced signal mimics the inverse beta decay [11].

- **Geo-neutrinos**: Radioactive decays within the earth producing antineutrinos can lead to inverse beta decay signals in the detector. Since, for the determination of the mass ordering, the distance L to the source is crucial, these signals muddle the desired spectrum.

To quantify the impact of the mentioned types of background, as well as to give an idea of the reduction of those backgrounds with the help of selection cuts, Table 3.3 is included. The details to each cut can be found in [11]. While the accidental background

Table 3.3: Efficiency of the selection cuts, as well as quantities for the signal and each background after each cut [11].

Selection	IBD eff.	IBD	Geo-νs	Accidental	^{9}Li/^{8}He	Fast n	α+^{13}C
-	-	83	1.5	$\sim 5.7 \times 10^{4}$	84	-	-
Fiducial volume	91.8 %	76	1.4	410	77	0.1	0.05
Energy cut	97.8 %	73	1.3		71		
Time cut	99.1 %						
Vertex cut	98.7 %			1.1			
Muon veto	83 %	60	1.1	0.9	1.6		
Combined	73 %	60	3.8				

has the highest occurrence, it is efficiently reducible to $\approx 3 \times 10^{-3}$ of its original count rate. The most efficiency is lost due to the muon veto, which is essential for reducing the cosmogenics background. The muon veto consists of the following cases [11]:

- A muon tagged by the water pool $\rightarrow$ The whole LS volume is vetoed for 1.5 ms.

- A muon that is well tagged in the water Cherenkov veto and the central detector $\rightarrow$ A cylindrical detector volume with $R < 3$ m around the track is vetoed for 1.2 s.
- A tagged, non-trackable muon in the central detector $\rightarrow$ The whole LS volume is vetoed for 1.2 s.

Reducing the volume and/or time these vetoes have to be applied, without loosing background suppression, can significantly increase the statistic JUNO can accumulate.

Chapter 4

Topological Track Reconstruction

Developed for large-volume liquid scintillator experiments, the Topological Track Reconstruction (TTR) utilizes the time-information of the detected scintillation light to draw inferences about the topology of the event's light emission. Its original purpose is the reconstruction of hadronic showers along muon tracks to reduce vetoed detector space and therefore increase efficiency.
The TTR requires only few assumptions: A point in space is known, at which the particle was located at a known time (called reference point and reference time) and that the particle travels through that reference point on a straight track with the speed of light in vacuum. Under these assumptions, the time t_{signal} it takes for an unscattered scintillation photon to reach a PMT can be described by [22]

$$t_{signal} = \frac{1}{c} \cdot \left(\left| \overline{VX} \right| \pm n \cdot \left| \overline{XP} \right| \right) \tag{4.1}$$

as the sum of the time it takes the particle to travel from the reference point V to the point of emission X and the time it takes the scintillation light to travel from the point of emission to the PMT position P, as visualized in Figure 4.1. The $\pm$ in Equation 4.1

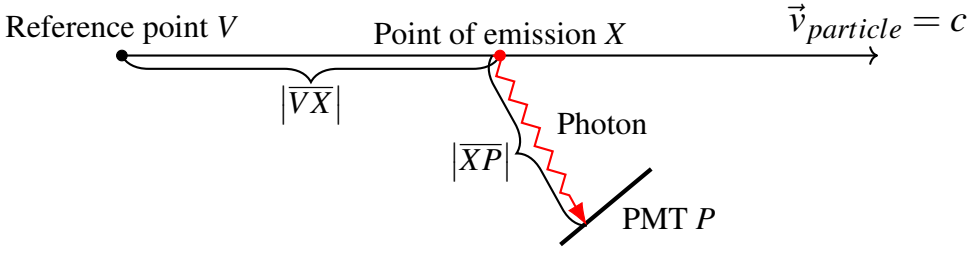

Figure 4.1: Illustration of the physics of Equation 4.1. A transiting particle with velocity and direction $\vec{v}_{particle}$ induces the emission of a scintillation photon at point $\boldsymbol{X}$ at a distance of $\left|\overline{VX}\right|$ to the reference point $\boldsymbol{V}$. The photon then hits a PMT $\boldsymbol{P}$, after traveling the distance $\left|\overline{XP}\right|$ through the detector.

depends on whether the emission at X happened after (+) or before (-) the reference time. Solving this equation results in a sharp isochronous surface on which possible

points of emissions for the individual PMT-hit are located. Examples for different times t_{signal} for both cases are presented in Figure 4.2. In reality, the time the scintillation light

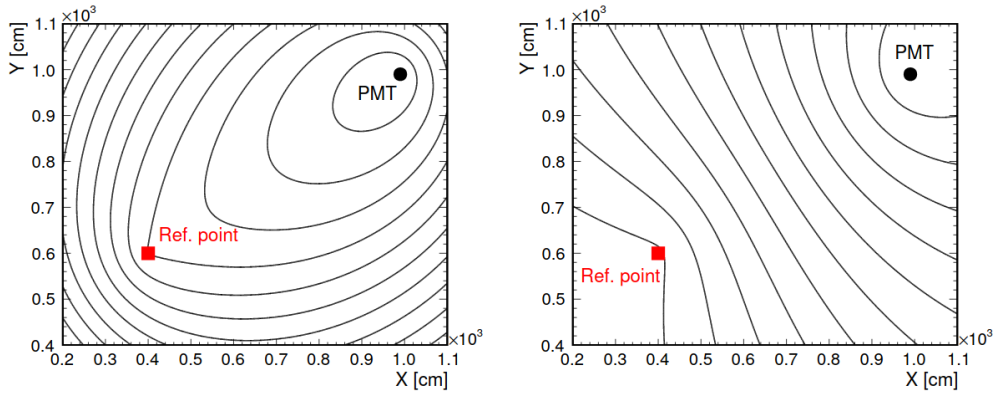

Figure 4.2: Two-dimensional isochrones in the LENA-detector for different values of t_{signal} as given by eq:travelTime, with a plus sign (left) and a minus sign (right) [12].

takes to hit the PMT is described by a time distribution because statistical processes like the emission of scintillation light and the time resolution of the PMT are involved and produce an uncertainty. In the TTR the time distribution

$$F(t) = \sum a_i \cdot \frac{1}{\tau_i \cdot 2} \cdot e^{-\frac{1}{\tau_i}\left((t - t_{signal} - \frac{\sigma^2}{\tau_i 2}\right)} \cdot \left[1 + \mathrm{erf}\left(\frac{(t - t_{signal}) - \frac{1}{\tau_i}\sigma^2}{\sqrt{2}\sigma^2}\right)\right] \tag{4.2}$$

is calculated as the convolution of the exponential scintillation spectrum and the Gaussian TTS of the PMTs, where τ_i is the i-th half-life of the scintillator and a_i is the fraction of the corresponding decay component with $\sum_i a_i = 1$ [22]. The error function hereby suppresses the exponential function for $t < t_0$, since the exponential decay starts at t_0 and therefore values before that point are nonsensical. Applying this equation to the concept presented above, a probability density distribution $P(\vec{x})$ based on t_{signal} is obtained

$$P(\vec{x}) = F(t(\vec{x})) = F\left(\frac{1}{c_0} \cdot \left(\left|\overrightarrow{Vx}\right| + n \cdot \left|\overrightarrow{xP}\right|\right)\right), \tag{4.3}$$

producing a washed out isochrone instead of a sharp one. This probability density however does not take effects like the attenuation within the detector or limitations of detection efficiency of the PMTs, e.g. due to angular acceptance, into account. Therefore the local detection efficiency $LD(\vec{x})$ is introduced and Equation 4.3 is modified to

$$P(\vec{x}) = F(t(\vec{x})) \cdot LD(\vec{x}) \tag{4.4}$$

to include a factor that allows for these effects. In Figure 4.3 the difference of Equation 4.3 and Equation 4.4 is visible. On the left, the initially sharp isochrone resulting from Equation 4.1 (solid black line) is washed out and a drop-like probability distribution describes the scintillation emission probability. On the right, the local detection

efficiency limits the possible area of emission and the attenuation pulls the probability closer to the PMT. With the purpose of weighing each PMT-hit in an event as such, a

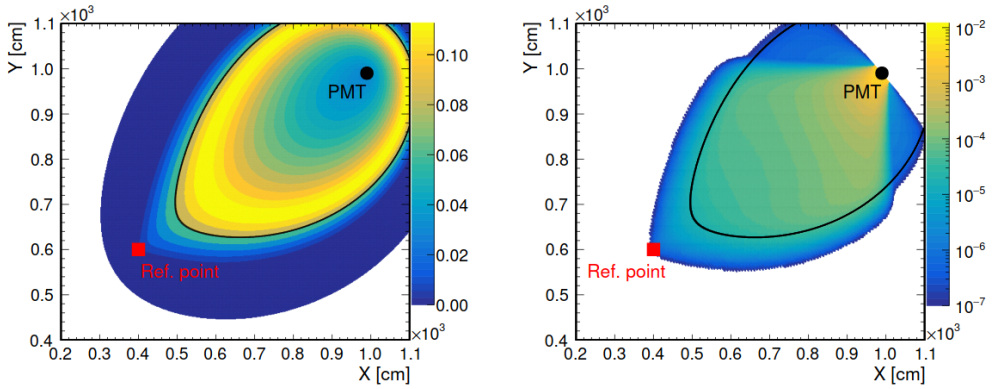

Figure 4.3: Unnormalized two-dimensional probability density distribution in the LENA-detector without (left, Equation 4.3) and with (right, Equation 4.4) the inclusion of the local detection efficiency. The black line indicates the sharp isochrone given by Equation 4.1 [12]

single hit, Equation 4.4 is normalized:

$$P(\vec{x}) = \frac{F(t(\vec{x})) \cdot LD(\vec{x})}{\int\int\int F(t(\vec{x})) \cdot LD(\vec{x}) \cdot d\vec{x}} \tag{4.5}$$

Now, the probability density distributions for each PMT-hit can be combined, overlapping them, to receive the 3D topology of the event. As the origins of the detected photons are unknown, the PMT-hits have to be treated as independent and the probability density distributions need to be summed up

$$P(\vec{x}_{total}) = \sum_i P_i(\vec{x}) = \sum_i \left[\frac{F_i(t(\vec{x})) \cdot LD_i(\vec{x})}{\int\int\int F_i(t(\vec{x})) \cdot LD_i(\vec{x}) \cdot d\vec{x}} \right], \tag{4.6}$$

where i describes the individual signals [22]. With Equation 4.6 a 3D representation of probability distribution of photons detected at each point in the detector is possible. To reconstruct the event topology, the emitted photons are required instead of the detected photons. This is achieved by weighting the number of detected photons with the inverse of total signal detection efficiency $\eta(\vec{x})$:

$$\langle N_{emitted}(\vec{x}) \rangle = \frac{\langle N_{detected}(\vec{x}) \rangle}{\eta(\vec{x})} = \frac{P(\vec{x}_{total})}{\sum_{PMT} LD_{PMT}(\vec{x})} \tag{4.7}$$

Knowing that the photons are correlated, as they belong to the same event, a so called probability mask PM($\vec{x}$) is introduced. This probability mask consists of a weight allocated to each voxel in the detector, reflecting the probability that a photon emitted at that point is part of the event topology of interest. To accommodate this probability mask,

Equation 4.4 is modified:

$$P(\vec{x}) = \frac{F(t(\vec{x})) \cdot LD(\vec{x}) \cdot PM(\vec{x})}{\int\int\int F(t(\vec{x})) \cdot LD(\vec{x}) \cdot d\vec{x} \cdot PM(\vec{x})}. \tag{4.8}$$

Making the TTR an iterative method, the first significant probability mask used is the result of the first iteration, which is working without a uniform mask. Afterwards each iteration uses its prior result as its probability mask. With this, an accurate and robust reconstruction of the event topology is achieved over the course of around 10 iterations for point-like events and around 20 iterations for muon tracks. An example of the results of this process is presented in Figure 4.4, showing a slice of the detector volume for 0, 8 and 21 iterations over a muon event. The method finds the area of interest with the uniform probability mask and hones in on the event topology, here the original track shown in red, over the iterations. After the iterative process, the event topology is reconstructed with a resolution of ≈ 10 cm.

The NLL algorithm introduced in this bachelor thesis aims at improving the TTR. One of the goals of the introduction of the negative logarithmic likelihood algorithm is its potential use as a criterion of termination for the iterative loop, which it currently lacks. Missing a criterion for the termination can lead to overfitting, reducing the accuracy of the reconstruction with higher iterations.

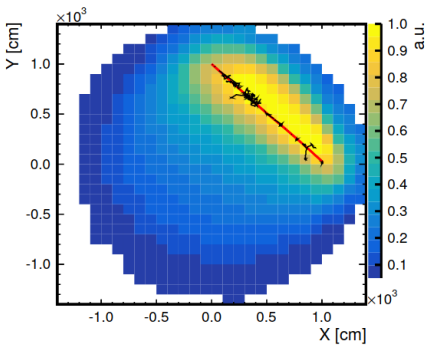

(a) Iteration 0.

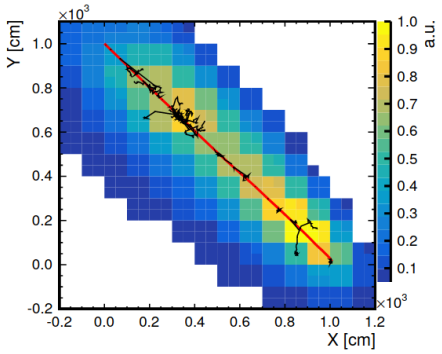

(b) Iteration 8.

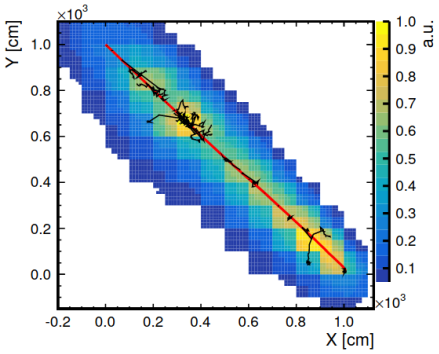

(c) Iteration 21.

Figure 4.4: Results of the reconstruction after different iteration steps, for a simulated 3 GeV muon in the cylindrical LENA detector. The red line indicates the track of the primary particle, while the black lines show secondary particles [12].

For a more detailed explanation of this method, consider reading [22] or [12], whose contents have been summarized here.

Chapter 5

Application of the negative logarithmic likelihood to the 3-D topological reconstruction in JUNO

5.1 Negative Logarithmic Likelihood

Likelihood functions are used to determine the quality of a fit. They determine which parameters best match the mathematical description of the case of interest. For a probability density function $P_\eta(x)$, with variable x and dependant on a parameter η, the likelihood function is defined as:

$$\mathbf{L}_x(\eta) = P_\eta(x), \tag{5.1}$$

treating the parameter of the probability density function as a variable and its variable as a parameter. A tangible explanation would be that the likelihood function treats the hypothesis as the truth and finds under which parameter η it best fits the observed value at x. If a specific parameter η is proposed, a high likelihood means a good agreement between hypothesis and measurement, while a low likelihood expresses the opposite.
The Negative Logarithmic Likelihood (NLL) is then defined as the negative of the logarithm of a likelihood function:

$$\mathscr{L}_x(\eta) = -\ln(\mathbf{L}_x(\eta)) = -\ln(P_\eta(x)). \tag{5.2}$$

This means that the logarithms of independent probabilities can be summed instead of multiplied for a total probability (Equation 5.3), which is faster and easier to handle for computers.

$$\mathscr{L}_{x,tot}(\eta) = -\ln\left(\prod_i P_\eta(x_i)\right) = -\sum_i \ln\big(P_\eta(x_i)\big) \tag{5.3}$$

Since the inserted probabilities $P_\eta(x)$ will be between zero and one, their logarithm $\ln(P_\eta(x))$ will result in values between negative infinity and zero, with higher negative values corresponding to lower probabilities. Since computers are faster at finding minima instead of maxima, the negative of these values is taken, leaving positive values between zero and infinity, with a lower NLL corresponding to a higher probability.

5.2 Motivation

This thesis deals with the implementation of the NLL method into the TTR. The main goal being the testing of the NLL as a means of improving the TTR overall in the future. The goal of this thesis will be the study of the NLL method as a quantitative criterion of termination for the iterative process of the TTR (chapter 4), as well as its properties as a quantifiable measure of quality for the reconstruction. On top of that, the NLL holds the potential of improving the vertex reconstruction for point-like events. Future applications can also include the alternating iteration of the TTR and the NLL, in which case the bin content of some bins can be adjusted to minimize the NLL before returning to another iteration of the TTR, improving the probability mask. Implementing a measure of quality for the TTR will allow for an easier assessment of its accuracy and the impact of potential changes. Establishing a well-founded criterion of termination will increases the efficiency of the reconstruction, as time is saved when further iterations only lead to negligible improvement or if they are detrimental, for example by overfitting or enhancing artifacts. In addition, the change of the quality over each iteration can be monitored, increasing the robustness of the TTR, as a (continual) decrease of the NLL is easily noticeable.

Improving the accuracy of the TTR and the vertex location can improve particle identification methods for low energy events (< 10 MeV), for example the recently presented electron-positron discrimination [10]. For high energy events it also provides the possibility of dampening or removing background which is otherwise difficult to separate from the signal, like the neutral current background in LS long baseline neutrino experiments, which is explained in more details in a later paragraph. Additionally, an accurate reconstruction allows minimizing the vetoes imposed on the detector for cosmogenics produced by transiting muons. This can increase the signal statistic as more detector volume becomes available for measurements.

Differentiating a low energy electron and a low energy positron is a difficult task in a liquid scintillator detector, as the reconstructed probability density for low energy events is a diffuse cloud around the actual vertex. A recent approach utilizing the TTR shows promising results, comparing the topological signature of reconstructed electron and positron events. The method uses the so-called radial event profile, which is established by beginning with the maximum bin within the diffuse cloud and then, going radially

outward, calculating the average bin content for each radius. Different criteria of differentiation are established based on the radial event profile. One of these criteria is based on comparing the derivative of the radial event profile of electron and positron events, where a difference can be established, as the positron clouds tend to be more diffuse due to the annihilation of the positron into two gammas, which move away from the center while producing scintillation light. This results in a more shallow flank for positron events [10]. The difference in steepness can then be used to discriminate the two event types. Improvements of the TTR could help improve this method, as a more accurate vertex location helps to center the radial event profile on the actual vertex, increasing its overlap with the event. Moreover, a general increase in accuracy of the reconstructed event topology could allow for a higher degree of separation between positron and electron events, as the steepness of the slope of point-like events would be more pronounced. Ideally, future resolutions allow the identification of the individual gammas of the event. This would allow for an easier, more efficient electron-positron discrimination.

As mentioned, future application of the TTR can also include long baseline LS neutrino detectors and it is therefore important and interesting to consider applications that go beyond the current application for JUNO. Long baseline neutrino experiments are set up to use a high flux $\nu_\mu/\bar{\nu}_\mu$ neutrino beam as their source, placing the detector at a distance L to the beam which maximizes sensitivity of the desired parameters. With this, appearance or disappearance experiments can be performed. Interfering at $\nu_e/\bar{\nu}_e$ appearance experiments, the source of neutral current background is the production of π^0 in neutral current processes that don't result in additional leptons. The resonant pion production

$$\nu_l(\bar{\nu}_l) + N \rightarrow \nu_l(\bar{\nu}_l) + N + \pi^0, \tag{5.4}$$

where $l = e,\nu,\tau$ are the possible flavours and N is a nucleon, is responsible for the majority of the neutral pions [23]. With its mean life time of $\tau_{\pi^0} = (8.52 \pm 0.18) \times 10^{-17}$ s [4], the distance covered by the π^0 is so short that the assumption of a point-like decay is justified [23]. The π^0 decays into two gammas with a branching ratio of 98.8 % [4] [23],

$$\pi^0 \rightarrow \gamma + \gamma, \tag{5.5}$$

which is the channel responsible for the neutral current background. The energy of each of the gammas is $E_\gamma < m_{\pi^0}$, with the mass of the pion $m_{\pi^0} \approx 134.98$ MeV [4]. As the kinetic energy of the pion can be asymmetrically distributed between the gammas, the energy of each can only be expressed by an upper limit with the implication $E_{\gamma_1} + E_{\gamma_2} = m_{\pi^0}$. As the photons are strongly boosted in the flight direction of the π^0, due to the particles high momentum, it is possible that the gammas can not be recognized as separate particles in the detector. This results in a signal, which is difficult to distinguish from an electron event, as the signature of electrons and gammas are very similar [23]. Since $\nu_e/\bar{\nu}_e$ appearances are measured with channels involving electrons,

this inability to differentiate between gamma and electron is problematic. Future application of a more developed and improved TTR could be a way to counteract the NC-Background. If the TTR is precise enough it could be possible to separate the two gammas or at least have a consistent method of differentiating the π^0-decay from an electron.
For the TTRs application in JUNO, the cosmogenics Li^9 and He^8 are a major background source (Table 3.3), due to their difficult to determine point of origin and their non-negligible lifetimes. As cosmogenics are primarily produced in secondary vertices of muons tracks, a big volume around each track is usually vetoed for a significant duration (see Table 3.2). Improving the reconstruction of muon tracks can help to deploy more efficient vetoes. Under sufficient resolution, a reconstruction of the event topology of a muon track could allow the discernment of point of origin of secondary vertices and therefore enable vetoing only areas with a high probability of producing cosmogenics. This reduction of vetoed volume directly increases the statistic of the detector and therefore decrease the time span of its measurements. For this case, the NLL can either be used to determine the quality of future algorithms implemented to determine secondary vertices or be directly deployed to increase the precision of the TTR. Here, the alternation between the reconstruction and the NLL method, mentioned above, can be used to adjust the content of individual bins to maximize the NLL and therefore provide a better probability mask for further iterations.

5.3 Basic idea and implementation

The basic idea can be presented in form of a question: "If the reconstruction is true, how likely is it to see the detected hit times as well as the number of photon hits on each PMT?" We can answer this question using the NLL, which in this case can be separated into the charge-NLL $\mathscr{L}_{charge}$ and the time-NLL $\mathscr{L}_{time}$, due to their independent nature. As the final step, the combined NLL $\mathscr{L}_{combined}$ is obtained by summing up the charge-NLL and the time-NLL:

$$\mathscr{L}_{combined} = \mathscr{L}_{charge} + \mathscr{L}_{time}. \tag{5.6}$$

The process of calculating these two NLLs is discussed in section 5.3.1 and section 5.3.2. Since performing these calculations over a continuous detector volume would be impractical, the detector is divided into smaller uniform volumes, which will be referred to as bins. The value obtained in the center of each volume is representative for it as a whole and will be referred to as the content of the bin. In the application multiple Look-Up-Tables (LUTs) are used to reduce processing time. LUTs are 1- to 3-dimensional tables (or histograms), containing prior calculated or simulated data relevant for processes of interest. The mean detection probability for scattered and direct light of a

PMT at distance d and angle α, as well as the time distribution a PMT sees at distance d and angle α are saved in and read out of LUTs. The center of the coordinate system is placed in the center of the detector.

5.3.1 Charge-NLL

The charge-NLL represents the probability that the detected charge distribution is produced by the reconstructed event topology. Assuming the result of the reconstruction as the true event topology, the hits on each PMT are calculated. The result is a statistical charge distribution, which can then be compared to the measured distribution to determine the likelihood that the reconstruction accurately describes the original event. Its calculation can be broken down into the following steps:

1. Calculating the total charge on each PMT i, given the reconstruction.
2. Calculating the total probability $\mathrm{P}_{c,i}$ for each PMT i.
3. Calculating the NLL from the $\mathrm{P}_{c,i}$.

1. Total charge on a PMT: The total charge on a PMT i is the integral over the hits from each individual point $\vec{x}$ in the detector:

$$q_{rec,i} = \int A(\vec{x}) \cdot \varepsilon_i \cdot D_i(\vec{x})\, d\vec{x}, \tag{5.7}$$

where $A(\vec{x})$ is the result of the TTR at point $\vec{x}$, ε_i is the photo detection efficiency of PMT i and $D_i(\vec{x}) = D_{direct,}(\vec{x}) + D_{scatt,i}(\vec{x})$ is the combined detection probability for direct and scattered light, dependant on distance and angle between $\vec{x}$ to the PMT. For this, all PMTs, including the ones with no registered hit, are taken into account.

2. Calculating $\mathrm{P}_{c,i}$: The probability $P_{c,i}$ that the detected charge on a PMT $q_{det,i}$ is realised if the result of step 1 represents the event, can be calculated with a poisson distribution

$$P_\lambda(k) = \frac{\lambda^k}{k!} \cdot \exp(-\lambda), \tag{5.8}$$

with a parameter λ and a variable k and $\lambda, k \in \mathbb{R} \geq 0$. Hereby, the reconstructed charge is the parameter $\lambda = q_{rec,i}$ and the detected charge is the variable $k = q_{det,i}$.

3. Calculating the NLL: As a last step for the charge-NLL, the logarithm of each probability $P_{c,i}$ is formed, summed up and the result is multiplied by -1:

$$\mathscr{L}_{charge} = -\sum_i ln(P_{c,i}) \tag{5.9}$$

5.3.2 Time-NLL

The time-NLL represents the probability that the detected hit times stem from the reconstructed event topology. Its calculation can be broken down into the following steps:

1. Calculating the statistical time distribution the **i**th PMT detects from each point in the detector.

2. Calculating the complete statistical time distribution the **i**th PMT detects of the event.

3. Obtaining the probability $P_{t,i}$ for each hit time.

4. Calculating the NLL from the probabilities $P_{t,i}$.

1. Time distribution of each PMT for each point: Based on Equation 4.5, the statistical time distribution $T_{i,\vec{x}}(t)$ detected by a PMT i for each point $\vec{x}$ in the detector is described by a continuous, statistical spectrum. For this $T_{raw,\vec{x}}$, a hit time spectrum composed of the mean propagation time of photons of different wavelengths emitted at $\vec{x}$ and a spectrum of scattered light, is convolved with the time distribution of a hit $F(t)$, given by Equation 4.2 in chapter 4:

$$T_{i,\vec{x}}(t) = T_{raw,\vec{x}}(t) * F(t). \tag{5.10}$$

To account for the fact that the emission of photons is more probable at some points in the detector than at others, based on the event topology, the time distribution is weighted with the charge detected from point $\vec{x}$, calculated with Equation 5.7 :

$$T_{i,\vec{x},weighted}(t) = q_{rec,i} \cdot \frac{T_{i,\vec{x}}(t)}{\int T_{i,\vec{x}}(t)\, dt}. \tag{5.11}$$

2.Time distribution for each PMT for the event: Summing the individual weighted time distributions $T_{i,\vec{x},weighted}(t)$ results in a time distribution $T_{i,Event}(t)$ that describes the ith PMTs hit time spectrum for the entire event:

$$T_{i,Event}(t) = \sum_{\vec{x}} T_{i,\vec{x},weighted}. \tag{5.12}$$

3. Obtaining the probabilities $P_i(t_{i,hit})$: Normalized, the time distribution $T_{i,Event}(t)$ acts as a probability density function for the hit times detected by PMT i:

$$P_i(t) = \frac{T_{i,Event}(t)}{\int T_{i,Event}(t)\, dt} \tag{5.13}$$

Therefore, the probability that a hit time $t_{i,hit}$ registered by PMT i is associated with the reconstructed event topology is given by the value of Equation 5.13 at $t_{i,hit}$:

$$P_i(t_{i,hit}). \tag{5.14}$$

3. Calculating the NLL: The logarithm of each probability $P_{i,\vec{x}}(t_{i,hit})$ is formed, summed up and the result is multiplied by -1:

$$\mathscr{L}_{time} = -\sum_i ln(P_i(t_{i,hit})) \tag{5.15}$$

5.4 Results

All the results presented are based on simulated data sets that account for scattered light in the detector and the TTS of PMTs, but exclude dark hits and . In the following, events with an energy of $E_{Event} < 10$ MeV are referred to as low energy events.

5.4.1 Toy-Monte-Carlo point-sources

To test the functionality and accuracy of the charge- and time-NLL described in section 5.3, a toy-Monte-Carlo for point-sources was established and used. The charge and time distributions resulting from the simulated point-sources are compared to a distribution of a point-like event by calculating the NLL. The idea of this test is, that the NLL-method should be able to find the position of the actual vertex, as the charge and time distributions of a perfect point-source are similar to the near point-like low energy events. Therefore, a simulated point-source located closer to the true vertex should have a lower NLL, being a better fit to the simulated distribution, than the ones further away. In practice, a photon point-source is simulated at a point $\vec{x}$ in the detector and for that point, the charge- and time-NLL are calculated, allocating their result to the point $\vec{x}$. Iterating this process over all or parts of the detector volume results in a 3-D histogram that visualizes the likelihood of the vertex position in the detector. Resulting histograms should then show a likelihood minimum around the true vertex. Examples of results of this are given in figure Figure 5.1, Figure 5.2 and Figure 5.3.
In order to save time, only a part of the detector volume is used for the calculations. To get a realistic starting point while analysing the area of interest, a crude estimation of the vertex was implemented:

$$\overrightarrow{COC} = \frac{\sum_i \vec{p}_i \cdot q_{det,i}}{\sum_i q_{det,i}}, \tag{5.16}$$

where $\vec{p}_i$ is the position of PMT i and $q_{det,i}$ is the charge detected by PMT i. This vector describes the center of charge of an event and will be referred to as COC in the following

text. It's accuracy decreases with vertex locations closer to the edge of the detector, meaning usually a radial correction is desirable. This correction is not yet implemented, resulting in a big inaccuracy of up to 130 cm. As the COC is only used to reduce the considered detector volume to the area of interest this has no significant impact on the NLL, if the deviation is considered when choosing the size of the examined area around the COC.

To make sure the point-source emits an amount of photons similar to the simulated event, it was assumed to emit $\approx$ 12,000 photons/MeV, which is comparable to the actual photo emission in the LS. This is possible, since the energy of the simulated event is known.

As an example, resulting histograms from the same event are presented for the charge-NLL (Figure 5.1), time-NLL (Figure 5.2) and combined-NLL (Figure 5.3). The results are presented as slices of the X-Y-, X-Z- and Y-Z-plane through the true vertex of the event, which is marked with a red dot. The NLL was calculated for a 600 cm $\times$ 600 cm $\times$ 600 cm cubic volume, which is centered on the COC, marked with a green triangle. This cube is separated into 27,000 cubic bins, each being 20 cm $\times$ 20 cm $\times$ 20 cm. The bin with the lowest content, meaning the lowest NLL, is marked with a black cross. This minimum is defined by locating the bin with the lowest content and taking its center. Therefore, the accuracy is limited by the size of the bins. Implementing a weighted minimum, allowing the minimum to be located at any point between bins, could potentially reduce this problem. In all three images a NLL minimum around the true vertex is visible, representing the desirable outcome. While the charge-NLL is able to find general vertex location, the time-NLL is able to precisely pinpoint it in this sample. For this example, the combined-NLL is dominated by the time-NLL.

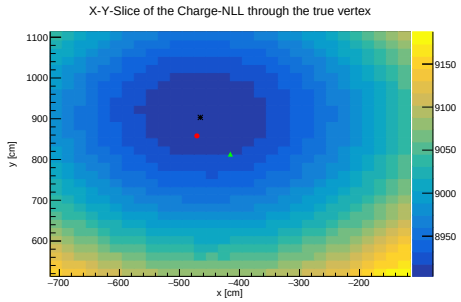

(a) Slice of the X-Z-plane of the Toy-Monte-Carlo charge-NLL.

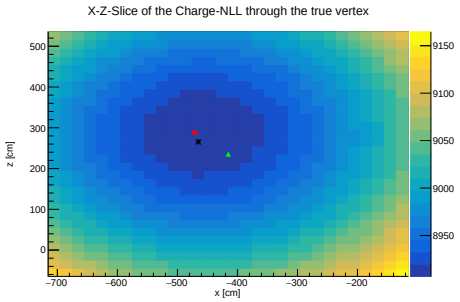

(b) Slice of the X-Z-plane of the Toy-Monte-Carlo charge-NLL.

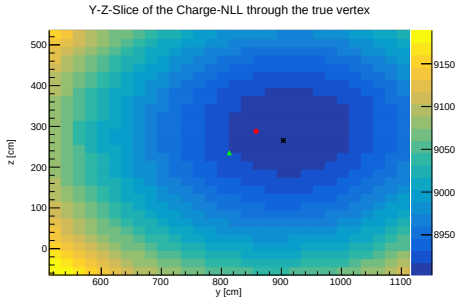

(c) Slice of the Y-Z-plane of the Toy-Monte-Carlo charge-NLL.

Figure 5.1: Result of Toy-Monte-Carlo charge-NLL for a 3 MeV electron event. The NLL is calculated for 27,000 bins (20 cm $\times$ 20 cm $\times$ 20 cm) over a range of $\pm$ 300 cm in each direction, centered on the COC. Red dot: True Vertex, Black cross: Minimum likelihood, Green triangle: COC.

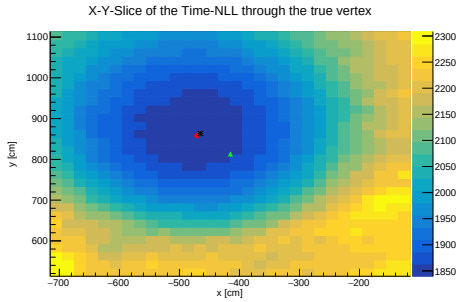

(a) Slice of the X-Z-plane of the Toy-Monte-Carlo time-NLL.

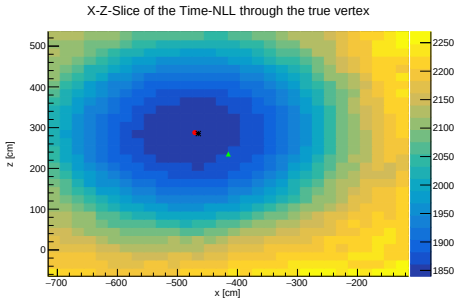

(b) Slice of the X-Z-plane of the Toy-Monte-Carlo time-NLL.

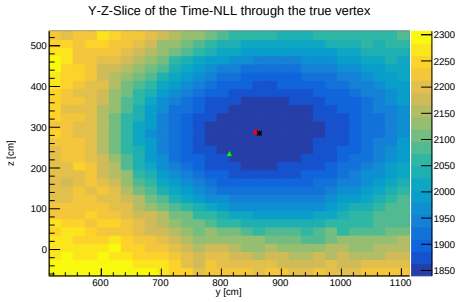

(c) Slice of the Y-Z-plane of the Toy-Monte-Carlo time-NLL.

Figure 5.2: Result of Toy-Monte-Carlo time-NLL for a 3 MeV electron electron event. The NLL is calculated for 27,000 bins (20 cm $\times$ 20 cm $\times$ 20 cm) over a range of $\pm$ 300 cm in each direction, centered on the COC. Red dot: True Vertex, Black cross: Minimum likelihood, Green triangle: COC.

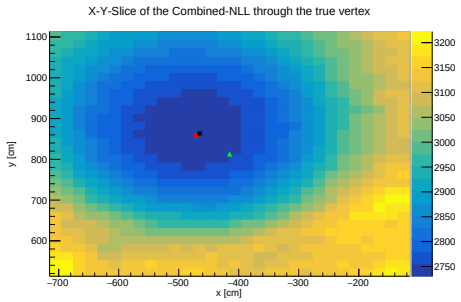

(a) Slice of the X-Z-plane of the Toy-Monte-Carlo combined-NLL.

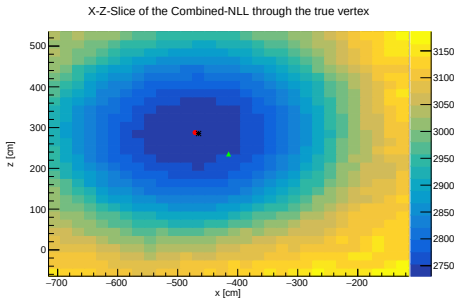

(b) Slice of the X-Z-plane of the Toy-Monte-Carlo combined-NLL.

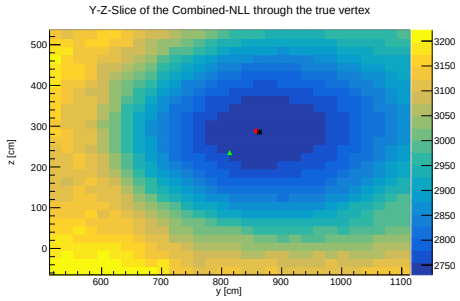

(c) Slice of the Y-Z-plane of the Toy-Monte-Carlo combined-NLL.

Figure 5.3: Result of Toy-Monte-Carlo combined-NLL for a 3 MeV electron event. The NLL is calculated for 27,000 bins (20 cm $\times$ 20 cm $\times$ 20 cm) over a range of $\pm$ 300 cm in each direction, centered on the COC. Red dot: True Vertex, Black cross: Minimum likelihood, Green triangle: COC.

The distances between true vertex and the bin with the NLL-minimum for this sample event are summarized in Table 5.1.

Table 5.1: Summary of the vertex resolution for a sample Event of a 3 MeV electron.

	ΔX	ΔY	ΔZ
charge-NLL	-5.7 cm	-45.3 cm	22.5 cm
time-NLL	-5.7 cm	-5.3 cm	2.5 cm
combined-NLL	-5.7 cm	-5.3 cm	2.5 cm

Following, the results of the charge- and time-NLL are discussed separately. Due to the simple nature of adding the result of the charge- and time-NLL , the combined-NLL is not given its own subsection.

Charge-NLL The charge-NLL was tested by determining its capabilities of finding the correct vertex position. This was done before the COC was implemented and instead the true vertex position was used as the center of the 3-D histogram. For this, the distance of the bin with the lowest charge-NLL to the true vertex was calculated and saved for each dimension ($\Delta X, \Delta Y, \Delta Z$). Testing if the method was able to find the general location of the vertex was successful in a small sample of events. These first results

were followed by a statistical analysis to determine the resolution. To increase resolution while keeping an acceptable run time of the method, the considered volume for the analysis was reduced to a 200 cm $\times$ 200 cm $\times$ 200 cm cube around the true vertex. The size of the volume was based off a conservative estimate of the resolution acquired in the manual analysis of the previous sample events. Segmenting the volume into 64,000 smaller volumes, 5 cm $\times$ 5 cm $\times$ 5 cm bins (40 along the length of each axis) were used. The bin size was chosen to be much smaller than the estimated resolution to not impose an artificial limit on it, while not being too small to maintain an acceptable run time. Using these configurations, the charge-NLL was calculated for a set of 10,000 3.5 MeV electron events, randomly located in the detector. Results are shown in Figure 5.4 for *X, Y, Z* as 1-D histograms fitted with a Gaussian using a fit function provided by ROOT [24]. A Gaussian fit, which is the theoretical expectation, is decently realised except for an excessive peak around 0 for all three directions. In all three histograms the maximum is located around 0, which is the desirable outcome. The accuracy of the method is similar for all directions but slightly worse in Z, summarized in Table 5.2. Visible in the histogram for ΔZ is that the higher deviations are more common than for ΔX and ΔY. Why the results for Z are slightly worse is unclear. A possible explanation is the asymmetry of the PMT distribution, as the acrylic sphere has an opening at the top, on its Z-axis, to fill and maintain the LS.

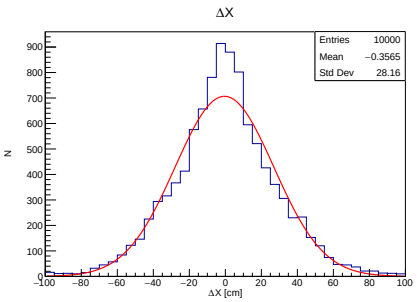

(a) Number of occurrences for different distances between X-Coordinate of the true vertex and minimum bin.

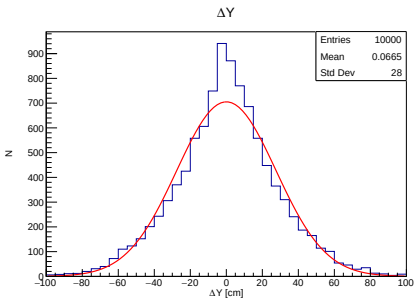

(b) Number of occurrences for different distances between Y-Coordinate of the true vertex and minimum bin.

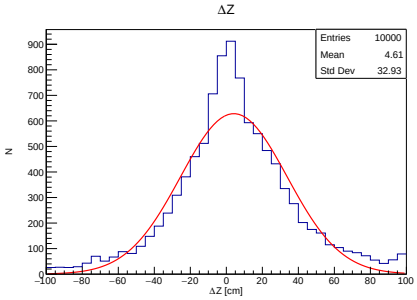

(c) Number of occurrences for different distances between Z-Coordinate of the true vertex and minimum bin.

Figure 5.4: Results of the statistical analysis of the charge-NLL for 10000 3.5 MeV electron events, fitted with a Gaussian.

Table 5.2: Summary of the vertex resolution of the charge-NLL.

Coordinate	Mean	1σ range
ΔX	-0.4 cm	28.2 cm
ΔY	0.1 cm	28 cm
ΔZ	4.6 cm	32.9 cm

Time-NLL To test the time-NLL, its behaviour is compared to the expected behaviour under correct implementation. As a first step for this, a point-like event and a single PMT located on the same axis of the detector were chosen to exploit the resulting symmetry of the NLL. Then, the PMT was artificially given hit times around the most probable hit time for the true vertex (Figure 5.6) as the detected hit time $t_{i,hit}$. With this artificial hit time, the expected result is a NLL minimum around the true vertex in the plane orthogonal to the symmetry axis. If the time is then adjusted by adding a few nanoseconds, the NLL distribution will change accordingly and turn into a ring around the vertex. This can be visualized by thinking of a washed out spherical surface representing the likelihood minimum spanned by the time-NLL. Hit times closer to the maximum result in a sphere with a radius similar to the distance of the PMT to the true vertex, therefore looking at a slice of the time-NLL distribution going through the true vertex, the expected results is disk around the true vertex. This disk is representing the cut through the sphere at a distance close to its radius. Ideally, the disk has a gradient of lower NLL values towards its center, as only the true vertex and its immediate surrounding is overlayed perfectly by the sphere. Hit times that are located after the maximum of the time distribution can be thought of as cuts of the sphere at a distance smaller than its radius, leaving a ring of its surface. The size of this ring will therefore change with the hit time given to the PMT, getting bigger for times after away from the maximum. Times before the maximum result in an increase in the NLL, as the sphere is not cut at all and therefore the probability at the true vertex is lower than at points closer to the PMT. Observing this behaviour in the implemented likelihood method shows whether the method works as intended or mistakes in the implementation have been made.
To demonstrate the time-NLL in this thesis, a sample event that was used to test the functionality is discussed. The true vertex of the event is located on the Z-axis ($\vec{V}$ = (0,0,-100) cm), with the chosen PMT also being located on the Z-axis ($\overrightarrow{PMT}$ = (0,0,-1950) cm). The time fed to the PMT as $t_{i,hit}$ is based on the time distribution the PMT detects from the point of the true vertex and is shown in Figure 5.6 and acquired by normalizing Equation 5.10

$$T_{PMT,\vec{V},Norm}(t) = \frac{T_{PMT,\vec{V}}(t)}{\int T_{PMT,\vec{V}}(t)\,dt}. \tag{5.17}$$

Beginning at 95.8 ns, before the maximum, $t_{i,hit}$ was increased in ten steps of 1 ns, reaching 104.8 ns located after the maximum. As seen in Figure 5.5, the time-NLL

has a disk-like minimum around the true vertex when given the most probable hit time (e). While the slices for the hit times before the maximum, especially (a) and (d), look similar to (a), the NLL values increase the lower the time. This is further visible due to the minimum bin. For (e) and (f), true vertex is found with a slight deviation, while for (a), (b), (c) and (d) the minimum is located far from the true vertex. Increasing the hit time beyond the maximum first leads to an expansion of the disk (f) until the likelihood minimum is described by a ring around the true vertex (g). With increasing hit time, the ring expands (h),(i),(j). The X-Z- and Y-Z-slices for each time can be found in the appendix (A).

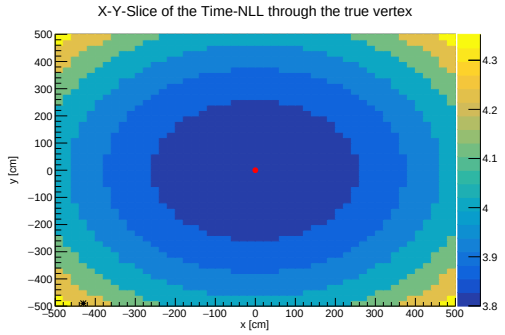

(a) Result of the time-NLL for $t_{i,hit}$ = 95.8 ns.

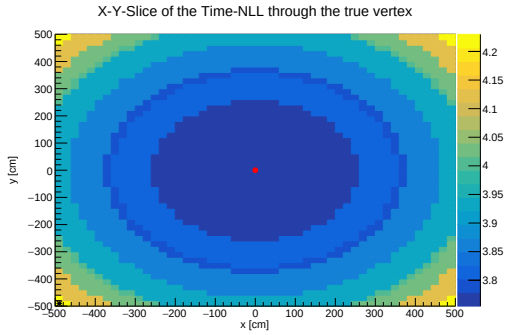

(b) Result of the time-NLL for $t_{i,hit}$ = 96.8 ns.

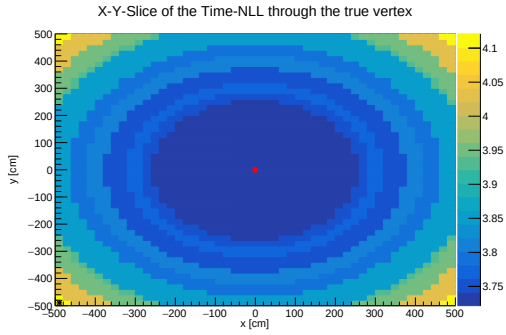

(c) Result of the time-NLL for $t_{i,hit}$ = 97.8 ns.

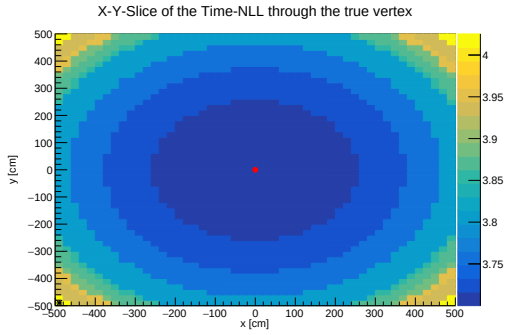

(d) Result of the time-NLL for $t_{i,hit}$ = 98.8 ns.

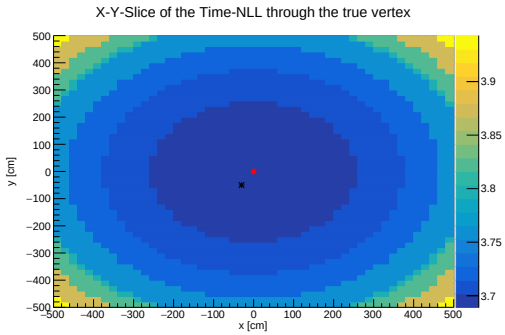

(e) Result of the time-NLL for $t_{i,hit}$ = 99.8 ns.

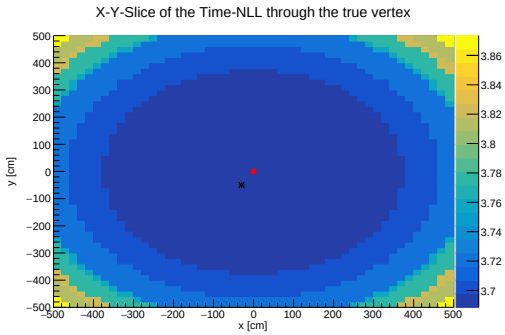

(f) Result of the time-NLL for $t_{i,hit}$ = 100.8 ns.

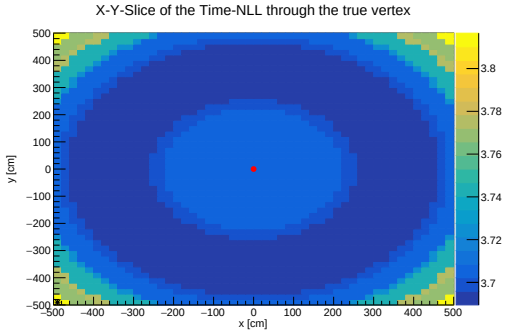

(g) Result of the time-NLL for $t_{i,hit}$ = 101.8 ns.

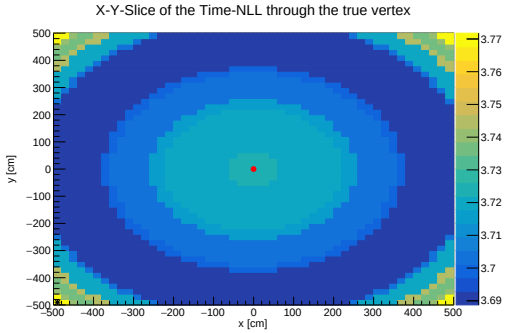

(h) Result of the time-NLL for $t_{i,hit}$ = 102.8 ns.

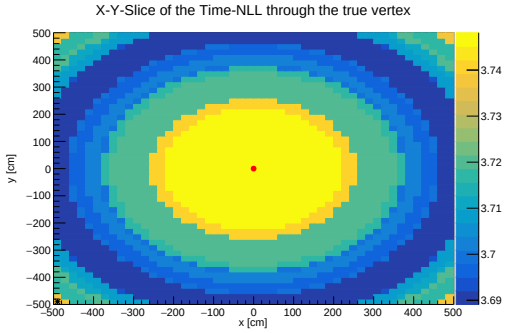

(i) Result of the time-NLL for $t_{i,hit}$ = 103.8 ns.

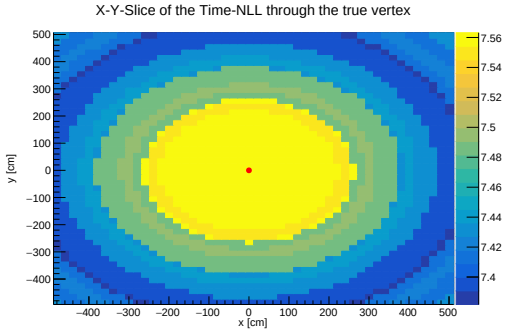

(j) Result of the time-NLL for $t_{i,hit}$ = 104.8 ns.

Figure 5.5: Results of the time-NLL test of a single PMT ($\overrightarrow{PMT}$ = (0,0, -1950) cm) for a 4 MeV electron event at $\vec{V}$ = (0,0,-100) cm). The PMT was manually given different $t_{i,hit}$. The true vertex is shown as a red dot. The bin with the minimum NLL is marked with a black cross.

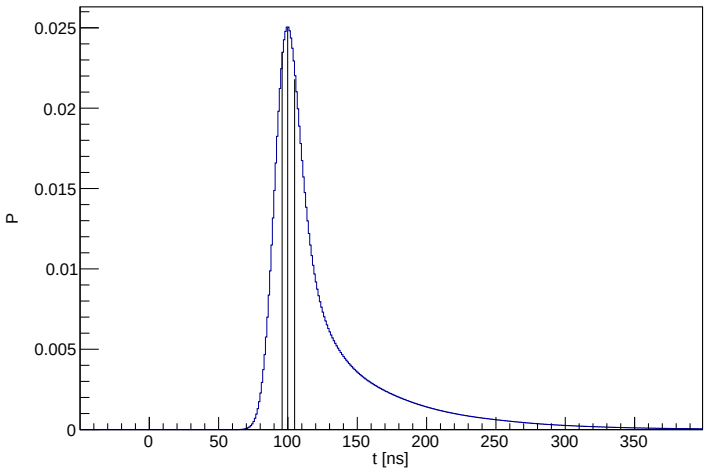

Figure 5.6: Time distribution detected from the true vertex $\vec{V}$ = (0,0,-100) cm by a PMT at $\overrightarrow{PMT}$ = (0,0,-1950) cm. The left and right vertical black line mark the beginning (95.8 ns) and the end (104.8 ns) of the looked at time span respectively. The black line in the middle marks the maximum of the distribution at 99.8 ns.

After confirming the expected behaviour of the time-NLL for a sample of events, all PMTs were used to without artificial hit times. Figure 5.7 shows the result of the time-NLL using all PMTs for the same event.

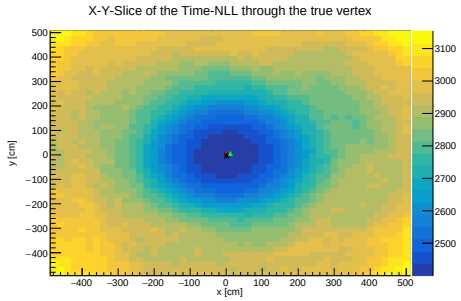

(a) Slice of the X-Z-plane of the Toy-Monte-Carlo time-NLL.

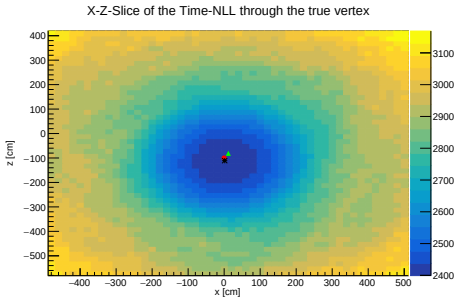

(b) Slice of the X-Z-plane of the Toy-Monte-Carlo time-NLL.

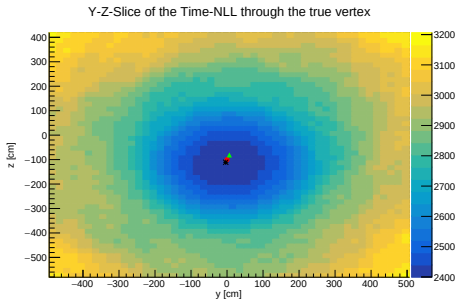

(c) Slice of the Y-Z-plane of the Toy-Monte-Carlo time-NLL.

Figure 5.7: Result of Toy-Monte-Carlo time-NLL for a 4 MeV electron event located at $\vec{V}$ = (0,0,-100). The NLL is calculated for 125,000 bins (20 cm $\times$ 20 cm $\times$ 20 cm) over a range of $\pm$ 500 cm in each direction, centered on COC. Red dot: True Vertex, Black cross: Minimum likelihood, Green triangle: COC.

As the run time of the time-NLL for one event is around 1 hour when using 20 $\times$ 20 $\times$ 20 bins, a statistical analysis with a large number of events has not been carried out. To estimate the vertex resolution of the time-NLL statistical analysis with a small batch of 100 3.5 MeV electron events, randomly located in the detector, was done. A 200 cm $\times$ 200 cm $\times$ 200 cm volume around the true vertex was used with 10 cm $\times$ 10 cm $\times$ 10 cm bins. Analogous to the charge-NLL, the distributions have been fitted with a Gaussian. With the low number of data points for the time-NLL, the Gaussian is mostly used to give an idea of the vertex resolution in this case.

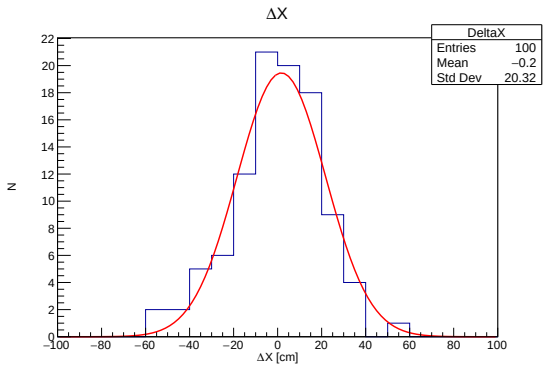

(a) Number of occurrences for different distances between X-Coordinate of the true vertex and minimum bin.

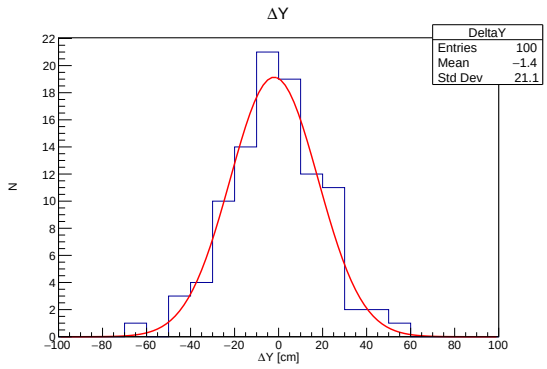

(b) Number of occurrences for different distances between Y-Coordinate of the true vertex and minimum bin.

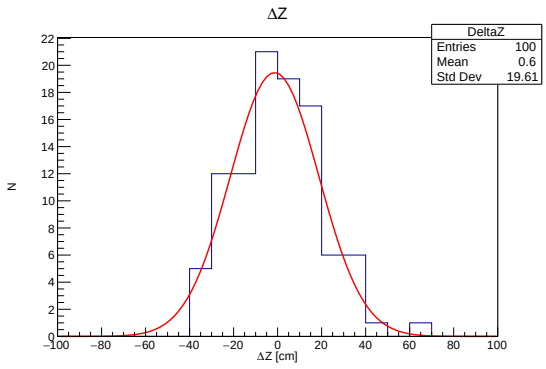

(c) Number of occurrences for different distances between Z-Coordinate of the true vertex and minimum bin.

Figure 5.8: Results of the statistical analysis of the time-NLL for 100 3.5 MeV electron events, fitted with a Gaussian.

Table 5.3: Summary of the vertex resolution of the time-NLL.

Coordinate	Mean	1σ range
ΔX	-0.2 cm	20.32 cm
ΔY	-1.4 cm	21.1 cm
ΔZ	0.6 cm	19.61 cm

5.4.2 Application to TTR results

After establishing and testing the NLL method with the help of the toy-Monte-Carlo point-sources introduced in section 5.4.1, it can be applied to the results of the TTR. For this a pair of a simulated event and its reconstruction with the TTR is taken. According to the description in section 5.3, the charge-, time- and combined-NLL are calculated. Doing this for all iterations of the TTR allows for the examination of the changes. Due to the long run time of the current version of the NLL-method no statistical analysis can be presented in this thesis. Two samples are provided for a 3.5 MeV electron event, Table 5.4, and a 1 MeV alpha event, Table 5.5. To reduce run time, the volume examined by the NLL method was reduced to 150 cm $\times$ 150 cm $\times$ 150 cm around the true vertex, corresponding to 12 bins with a volume of 12.5 cm $\times$ 12.5 cm $\times$ 12.5 cm. To make the difference in NLL easier to read $\Delta_{Combined}$ is introduced, defined as

$$\Delta_{Combined,i} = 100 \cdot \frac{\mathscr{L}_{combined,i} - \mathscr{L}_{combined,i-1}}{\mathscr{L}_{combined,i-1}}, \tag{5.18}$$

where $\mathscr{L}_{combined,i}$ is the combined-NLL of iteration i. Therefore positive values of $\Delta_{Combined}$ correspond to a worsening and negative values correspond to an improvement of the TTR results. For the electron event, being a point-like event, the TTR was

Table 5.4: Summary TTR-application results of the NLL method for a 3.5 MeV electron sample event. For all iterations after the thick black line the TTR used the same volume, bin size and amount of bins.

Iteration	Charge-NLL	Time-NLL	Combined-NLL	$\Delta_{Combined}$
0	12696.7	18431.2	31127.9	-
1	17899.3	18482.1	36381.4	(+16.9%)
2	40388.1	18480.9	58869.0	(+61.8%)
3	21892.1	18479.2	40371.3	-31.4%
4	21429.4	18477.2	39906.6	-1.2%
5	21326.6	18475.4	39802.1	-0.3%
6	20868.2	18473.3	39341.4	-1.6%
7	20773.8	18471.5	39245.3	-0.2%
8	20321.9	18469.2	38791.1	-1.2%
9	20240.2	18467.4	38707.7	-0.2%
10	17430.6	18465.4	35896.0	-7.3%

stopped after its 10th iteration. For a complete overview, iteration 0 and 1 are included. Comparing them to iterations 2-10 is meaningless, as the volume, bin size and amount of bins differ greatly. Iteration 0 of the TTR begins with a 1770 cm $\times$ 1770 cm $\times$ 1770 cm cube and 18 $\times$ 18 $\times$ 18 bins, representing the entire detector. Iteration 1 then limits the volume to a smaller cube, $\approx$ 786 cm $\times$ 590 cm $\times$ 590 cm, around the barycenter. The barycenter can be explained as a more complex version of the COC achieving accuracies of vertex locations of around 20 cm. This volume is separated into only 8 $\times$ 6

$\times$ 6 bins. Beginning with iteration 2, the volume, bin size and amount of bins stays constant, meaning that the difference in NLL between each iteration can be used as an indicator of quality improvement or deterioration. Iteration 2-10 use the same volume as iteration 1, but are instead separating it into 64 $\times$ 43 $\times$ 43 cubic bins with an edge length of 12.5 cm. Looking at iteration 2-10 in Table 5.4, a consistent decrease in the NLL with each iteration is visible. Especially the first iteration with uniform volume, bin size and amount of bins, from iteration 2 $\rightarrow$ 3, results in a significant drop of the NLL. After iteration 3 a pattern is visible, as every other iteration leads to a decrease much larger than its predecessor. This difference, of approximately a factor 4, continues until iteration 10, where another significant drop in the NLL occurs. A likely explanation of this pattern is the alternation between PMTs with even IDs and odd IDs in the TTR, when iterating. Alternating between the even and odd numbered PMTs helps to prevent self-enhancement of erroneous areas, as PMTs are not fed their own data as a probability mask. This sample event seems to show the desired outcome, as results of subsequent iterations lower the NLL and therefore match the event better. To visualize the improvement of the reconstruction, slices of the X-Y-plane running through the true vertex of the reconstructed event topology are presented in Figure 5.9 for iteration 2, 6 and 10. The corresponding slices of the X-Z- and Y-Z-plane can be found in the appendix. (A).

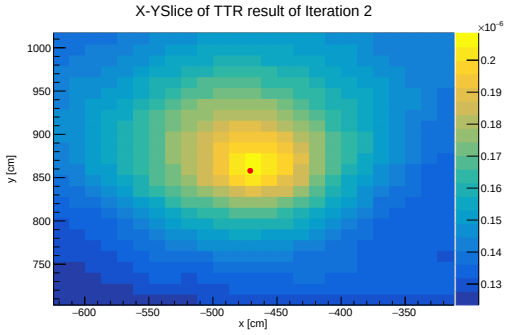

(a) Iteration 2.

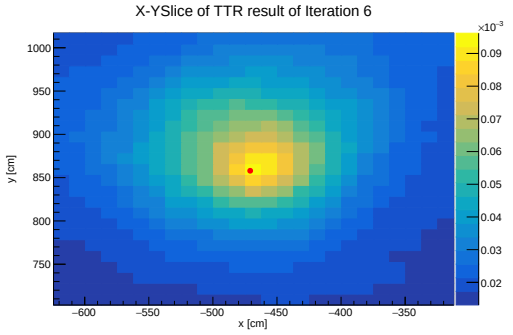

(b) Iteration 6.

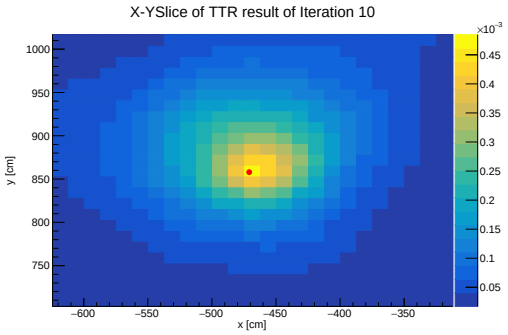

(c) Iteration 10.

Figure 5.9: X-Y-slices of TTR results of a 3 MeV electron event for different iterations. The true vertex is marked with a red dot.

The alpha event was chosen to represent an erroneous reconstruction of an event. The

reconstruction of the simulated 1 MeV alpha event resulted in an artifact, a miss placed maximum, that was contrasted more in comparison to the position around the true vertex with increasing iterations. This is visible in the X-Y-slices of the reconstructed topology, presented for iterations 2, 6, 8 and 9. Hereby the artifact most distinct in iteration 9, which is the final iteration of the events reconstruction. The slices of the X-Z- and Y-Z-plane can be found in the appendix (A).

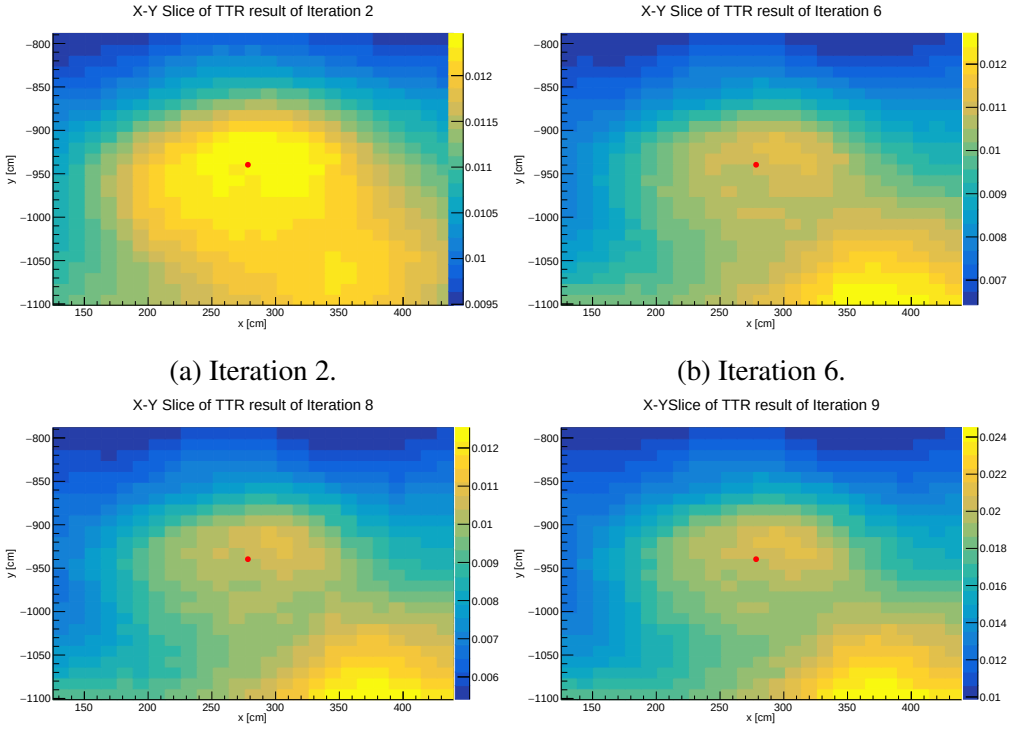

(a) Iteration 2.

(b) Iteration 6.

(c) Iteration 8.

(d) Iteration 9.

Figure 5.10: X-Y-slices of erroneous TTR results of a 1 MeV alpha event for different iterations. The true vertex is marked with a red dot.

The charge-, time- and combined-NLL for each iteration are summarized in Table 5.5. As iteration 0 and 1 are not comparable to iteration 2-9, the extreme behaviour between iterations 0-3 can be disregarded for this sample analysis. For iterations 2-8, the combined-NLL is decreasing slowly despite the artifact. This can be explained by the relative nature of the analysis. While the event is not reconstructed well, the topology presented by an iteration still describes the true event topology better than its predecessor. A significant jump (+45.4%) of the combined-NLL can then be observed going from iteration 8 to 9. This can be understood by looking at Figure 5.10. While (c) and (d) differ only slightly visually, a notable increase in emission probability, by a factor of 2, is recognizable in the color scale. This increase stems from the probability mask, reducing the volume in which light emission is assumed. Due to the limitation to a 150 cm $\times$ 150 cm $\times$ 150 cm cube around the true vertex, this constriction of the emission probability is only visible as an increase of the emission probability in the visible volume.

Table 5.5: Summary TTR-application results of the NLL method for a 1 MeV alpha sample event. For all iterations after the thick black line the TTR used the same volume, bin size and amount of bins.

Iteration	Charge-NLL	Time-NLL	Combined-NLL	$\Delta_{Combined}$
0	10274.5	10272.8	20547.3	-
1	$4.78128 \times 10^6 2$	10275.7	4.79155×10^6	(+23219.6%)
2	17576.2	10330.8	27907.0	(-99417578.9%)
3	16170.2	10330.8	26501.0	-5.0%
4	16085.5	10331.2	26416.8	-0.3%
5	14842.7	10331.2	25173.9	-4.7%
6	14743.3	10331.5	25074.9	-0.4%
7	13641.3	10331.4	23972.7	-0.4%
8	13555.9	10331.7	23887.5	-0.4%
9	24390.1	10331.7	34721.7	+45.4%

Chapter 6

Conclusion

In this thesis, the NLL-method was established for use in the TTR in the JUNO detector, to allow the evaluation of the quality of TTR results. It does so, by giving a quantitative measure of how likely the detected event signature is, given the reconstructed event topology. The NLL-method can therefore be used as a measure of quality of the TTR, as well as a quantitative criterion of termination of the iterative process. Furthermore, future applications can help to improve the TTR results by adjusting the probability mask between iterations, based on minimizing the NLL. For the implementation, the NLL was separated into the charge- and time-NLL, describing the charge distribution and time distribution produced by an event, respectively. The sum of the two NLLs defines the combined-NLL. For the purpose of testing the functionality of the method, a toy-Monte-Carlo simulation for point-sources was created. It was used to determine the resolution at which the charge-, and time-NLL can find the vertex for point-like events and to compare the behaviour of the time-NLL with its expected behaviour under correct implementation. Lastly, the NLL-method was applied to results of the TTR.
Implementation of the NLL-method in this thesis demonstrates its use as a measure of quality, criterion of termination and its potential for improving the TTR in the future. Testing of the charge- and time-NLL with the toy-Monte-Carlo point-sources was successful. Both methods showed behaviour that matched the expected behaviour under correct implementation. The tests with the toy-Monte-Carlo point-sources also showcase the possible application as a method for vertex reconstructions of point-like events. Using just the charge-NLL allows for a limitation of the vertex location, with a resolution of ≈ 30 cm in each direction (Table 5.2). Indicated by the analysis of 100 events, the time-NLL can resolve the true vertex with a resolution of ≈ 20 cm. Carrying out an analysis of the time-NLL with a larger number of events while using finer binning would lead to a more conclusive statement about its capabilities. Adding coupling with other methods of vertex reconstruction in the future, e.g. by cross-checking results, could lead to better and more robust vertex reconstructions.
Application of the NLL-method on events reconstructed by the TTR shows promising

results. When used on a well reconstructed point-like event, the NLL showed a continuous improvement with each iteration, which is the expected and desirable outcome. Additionally, the development of the NLL over the iterations also resolved the alternating between even and odd numbered PMTs used by the TTR, as well as the switch to using all PMTs in the last iteration. Upon application on an erroneous reconstruction the NLL showed a significant drop in the last iteration, in which the artifact was most contrasted. Nevertheless, a statistical analysis is necessary to draw a meaningful conclusion as the sample results can be outliers.

In the future, the NLL-method can be improved further and even branched out, depending on its application. A sensible first step to improve the NLL-method will be a parallelization, which could easily reduce the run time by a factor 10, depending on how many cores are available to the program. This improvement is essential in the application of the method within the TTR, as the current run time would slow down the TTR significantly. Therefore, the application of the NLL-method as a measure of quality and a criterion of termination of the iterative process, while theoretically possible, would be impractical until this issue is resolved. Once the run time is reduced, the NLL-method can also be applied on more complex events like muon tracks. For this, another toy-Monte-Carlo, simulating a perfect track, could be used to first test the functionality. This is not strictly necessary though, as the application on the TTR results does not make any assumption about the track topology.

In this thesis a working NLL-algorithm, capable of being the basis for the discussed (section 5.2) short- and long-term applications, has been established, which can be implemented in the TTR software package in the future.

Bibliography

[1] K. Eguchi, S. Enomoto, K. Furuno, J. Goldman, H. Hanada, H. Ikeda, K. Ikeda, K. Inoue, K. Ishihara, W. Itoh, *et al.*, "First results from kamland: evidence for reactor antineutrino disappearance," *Physical Review Letters*, vol. 90, no. 2, p. 021802, 2003.

[2] Y. Abe, C. Aberle, T. Akiri, J. Dos Anjos, F. Ardellier, A. Barbosa, A. Baxter, M. Bergevin, A. Bernstein, T. Bezerra, *et al.*, "Indication of reactor ν e disappearance in the double chooz experiment," *Physical Review Letters*, vol. 108, no. 13, p. 131801, 2012.

[3] Wikipedia, the free encyclopedia, "Standard Model," 2020. [Online; accessed August 31, 2020].

[4] "Particle Data Group." `https://pdg.lbl.gov/index.html`. Accessed: 2020-09-04.

[5] B. Povh, K. Rith, C. Scholz, F. Zetsche, and W. Rodejohann, *Teilchen und Kerne: eine Einführung in die physikalischen Konzepte*. Springer-Verlag, 2013.

[6] N. Schmitz, "Neutrinophysik," 1997.

[7] M. Aker, K. Altenmüller, M. Arenz, M. Babutzka, J. Barrett, S. Bauer, M. Beck, A. Beglarian, J. Behrens, T. Bergmann, *et al.*, "Improved upper limit on the neutrino mass from a direct kinematic method by KATRIN," *Physical review letters*, vol. 123, no. 22, p. 221802, 2019.

[8] K. Collaboration, "KATRIN design report 2004," *FZKA report*, vol. 7090, 2005.

[9] K. Zuber, "Neutrino physics," 2004.

[10] H. Rebber, "Event Discrimination with Topological 3D Reconstruction at MeV Energies in the JUNO Experiment," 2020.

[11] F. An, G. An, Q. An, V. Antonelli, E. Baussan, J. Beacom, L. Bezrukov, S. Blyth, R. Brugnera, M. B. Avanzini, and et al., "Neutrino physics with JUNO," *Journal of Physics G: Nuclear and Particle Physics*, vol. 43, p. 030401, Feb 2016.

[12] B. S. Wonsak, C. I. Hagner, D. A. Hellgartner, K. Loo, S. Lorenz, D. J. Meyhöfer, L. Oberauer, H. Rebber, W. H. Trzaska, and M. Wurm, "Topological track reconstruction in unsegmented, large-volume liquid scintillator detectors," *Journal of Instrumentation*, vol. 13, no. 07, p. P07005, 2018.

[13] Wikipedia, the free encyclopedia, "Photomultiplier tube," 2020. [Online; accessed July 20, 2020].

[14] Hamamatsu Photonics, "MCP (Microchannel plate) and MCP assembly," 2020. [Online; accessed August 7, 2020].

[15] Z. Djurcic, X. Li, W. Hu, H. Gan, S. Dmitrievsky, K. Zhang, C. Fang, J. Fang, M. Xiao, L. Kang, *et al.*, "JUNO conceptual design report," tech. rep., 2015.

[16] T. Adam, F. An, G. An, Q. An, N. Anfimov, V. Antonelli, G. Baccolo, M. Baldoncini, E. Baussan, M. Bellato, *et al.*, "JUNO conceptual design report," *arXiv preprint arXiv:1508.07166*, 2015.

[17] Uni Mainz, "JUNO schematic," 2020. [Online; accessed Spetember 13, 2020].

[18] I. Esteban, M. Gonzalez-Garcia, A. Hernandez-Cabezudo, M. Maltoni, and T. Schwetz, "Global analysis of three-flavour neutrino oscillations: Synergies and tensions in the determination of θ 23, δ CP, and the mass ordering," *Journal of High Energy Physics*, vol. 2019, no. 1, pp. 1–35, 2019.

[19] "JUNO Purpose." `http://juno.ihep.cas.cn/Junojuno/Purjuno/201403/t20140306_117331.html`. Accessed: 2020-03-04.

[20] D. Meyhöfer, *3D Topological Reconstruction in JUNO applied to GeV events*. Dissertation, Universität Hamburg, 2020.

[21] Y. Abe, J. Dos Anjos, J. Barriere, E. Baussan, I. Bekman, M. Bergevin, T. Bezerra, L. Bezrukov, E. Blucher, C. Buck, *et al.*, "Improved measurements of the neutrino mixing angle θ 13 with the Double Chooz detector," *Journal of High Energy Physics*, vol. 2014, no. 10, p. 86, 2014.

[22] M. Meyer and K. Zuber, eds., *Proceedings, 5th International Solar Neutrino Conference: Dresden, Germany, June 11-14, 2018*, World Scientific, 2019.

[23] S. Lorenz, "Discrimination of Neutral Current Background in a Future Long-Baseline Experiment with LENA," diplomarbeit, Universität Hamburg, 2012.

[24] R. Brun and F. Rademakers, "Root—an object oriented data analysis framework," *Nuclear Instruments and Methods in Physics Research Section A: Accelerators, Spectrometers, Detectors and Associated Equipment*, vol. 389, no. 1-2, pp. 81–86, 1997.

Eidesstattliche Erklärung

Ich versichere, dass ich die beigefügte schriftliche Bachelorarbeit selbstständig angefertigt und keine anderen als die angegebenen Hilfsmittel benutzt habe. Alle Stellen, die dem Wortlaut oder dem Sinn nach anderen Werken entnommen sind, habe ich in jedem einzelnen Fall unter genauer Angabe der Quelle deutlich als Entlehnung kenntlich gemacht. Dies gilt auch für alle Informationen, die dem Internet oder anderer elektronischer Datensammlungen entnommen wurden. Ich erkläre ferner, dass die von mir angefertigte Bachelorarbeit in gleicher oder ähnlicher Fassung noch nicht Bestandteil einer Studien- oder Prüfungsleistung im Rahmen meines Studiums war. Die von mir eingereichte schriftliche Fassung entspricht jener auf dem elektronischen Speichermedium. Ich bin damit einverstanden, dass die Bachelorarbeit veröffentlicht wird.

Ort, Datum	Unterschrift

Appendices

Appendix A

Additional figures

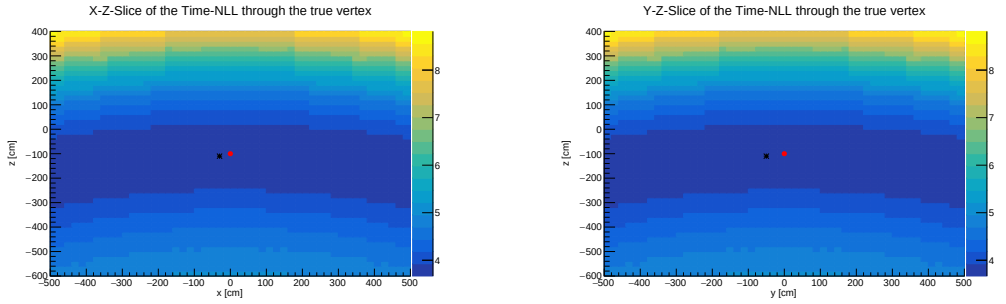

(a) Slice of the X-Z-plane.

(b) Slice of the X-Y-plane.

Figure A.1: Results of the time-NLL test of a single PMT ($\overrightarrow{PMT}$ = (0,0,-1950)) for a 4 MeV electron event at $\vec{V}$ = (0,0,-100). The PMT was manually given the hit time $t_{i,hit}$ = 99.8 ns. The true vertex is shown as a red dot. (Belongs to **??**)

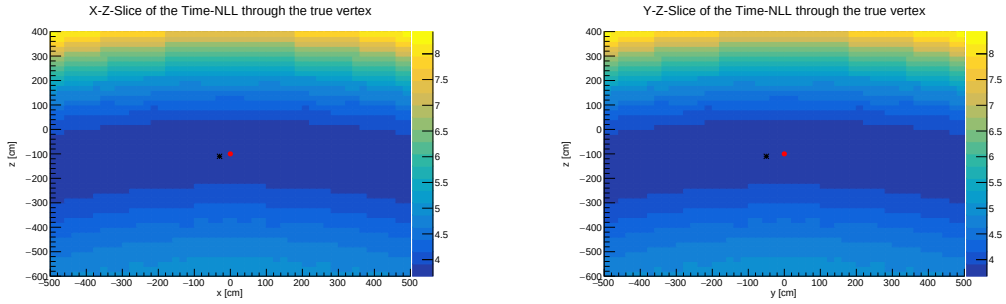

(a) Slice of the X-Z-plane.

(b) Slice of the X-Y-plane.

Figure A.2: Results of the time-NLL test of a single PMT ($\overrightarrow{PMT}$ = (0,0,-1950)) for a 4 MeV electron event at $\vec{V}$ = (0,0,-100). The PMT was manually given the hit time $t_{i,hit}$ = 100.8 ns. The true vertex is shown as a red dot. (Belongs to **??**)

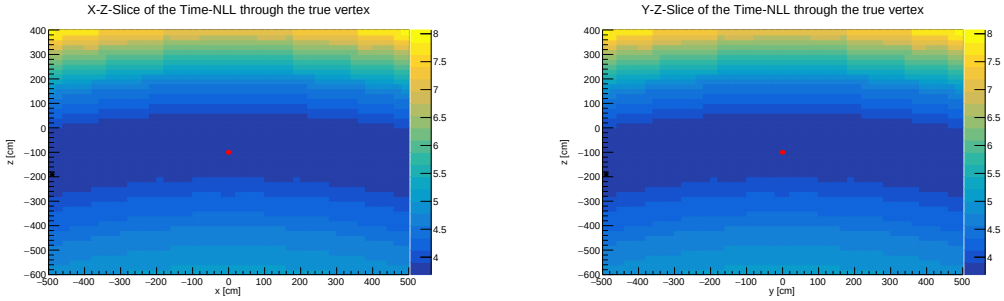

(a) Slice of the X-Z-plane. (b) Slice of the X-Y-plane.

Figure A.3: Results of the time-NLL test of a single PMT ($\overrightarrow{PMT}$ = (0,0,-1950)) for a 4 MeV electron event at $\vec{V}$ = (0,0,-100). The PMT was manually given the hit time $t_{i,hit}$ = 101.8 ns. The true vertex is shown as a red dot. (Belongs to **??**)

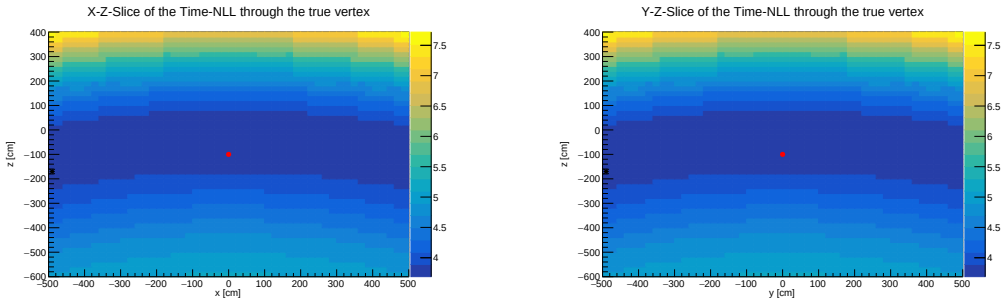

(a) Slice of the X-Z-plane. (b) Slice of the X-Y-plane.

Figure A.4: Results of the time-NLL test of a single PMT ($\overrightarrow{PMT}$ = (0,0,-1950)) for a 4 MeV electron event at $\vec{V}$ = (0,0,-100). The PMT was manually given the hit time $t_{i,hit}$ = 102.8 ns. The true vertex is shown as a red dot. (Belongs to **??**)

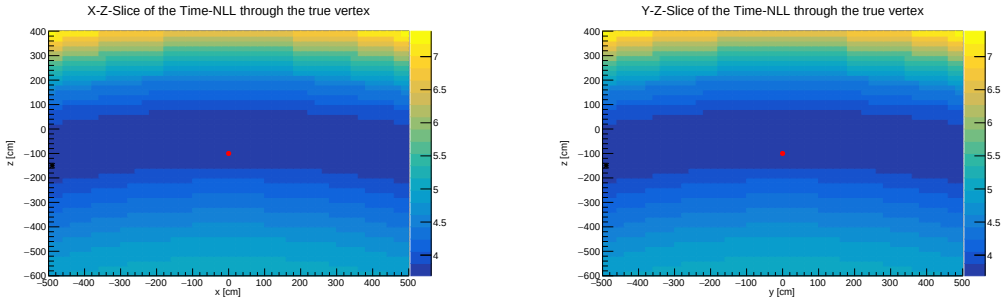

(a) Slice of the X-Z-plane. (b) Slice of the X-Y-plane.

Figure A.5: Results of the time-NLL test of a single PMT ($\overrightarrow{PMT}$ = (0,0,-1950)) for a 4 MeV electron event at $\vec{V}$ = (0,0,-100). The PMT was manually given the hit time $t_{i,hit}$ = 103.8 ns. The true vertex is shown as a red dot. (Belongs to **??**)

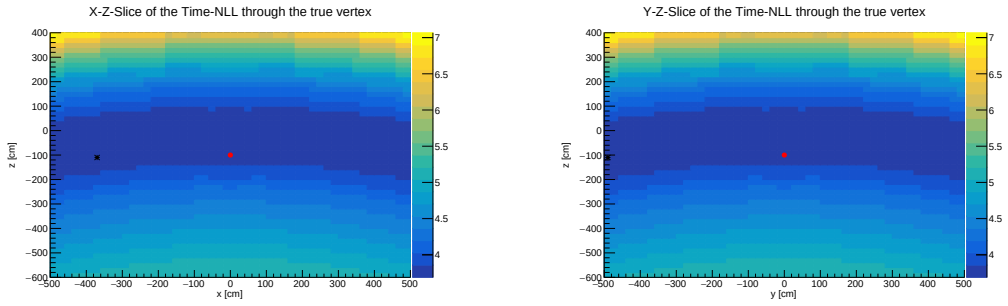

(a) Slice of the X-Z-plane. (b) Slice of the X-Y-plane.

Figure A.6: Results of the time-NLL test of a single PMT ($\overrightarrow{PMT}$ = (0,0,-1950)) for a 4 MeV electron event at $\vec{V}$ = (0,0,-100). The PMT was manually given the hit time $t_{i,hit}$ = 104.8 ns. The true vertex is shown as a red dot. (Belongs to **??**)

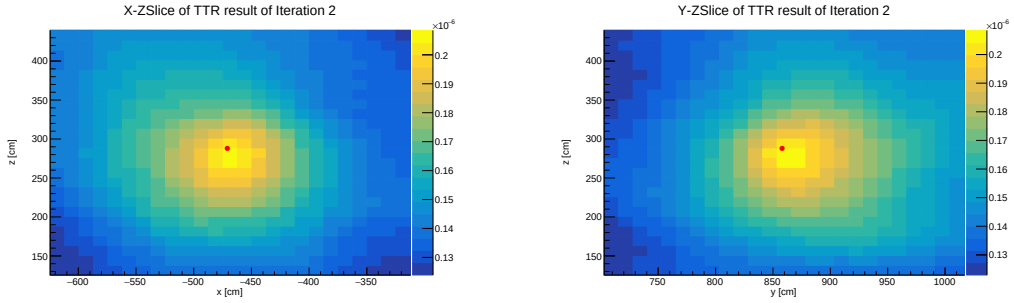

(a) Slice of the X-Z-plane. (b) Slice of the X-Y-plane.

Figure A.7: Slices of iteration 2 of TTR result for a 3 MeV electron event. The true vertex is marked with a red dot. (Belongs to Figure 5.9)

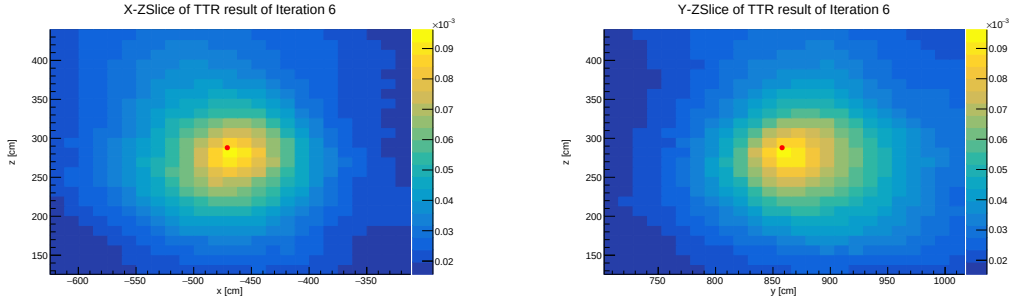

(a) Slice of the X-Z-plane. (b) Slice of the X-Y-plane.

Figure A.8: Slices of iteration 6 of TTR result for a 3 MeV electron event. The true vertex is marked with a red dot. (Belongs to Figure 5.9)

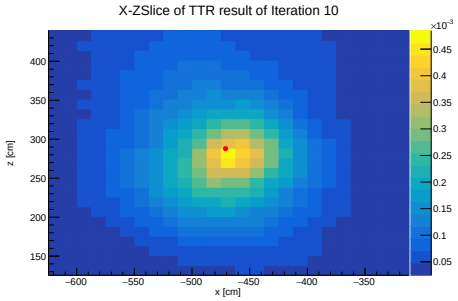

(a) Slice of the X-Z-plane.

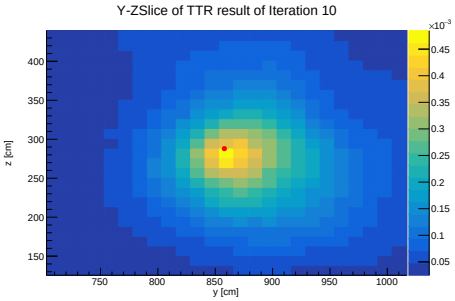

(b) Slice of the X-Y-plane.

Figure A.9: Slices of iteration 10 of TTR result for a 3 MeV electron event. The true vertex is marked with a red dot. (Belongs to Figure 5.9)

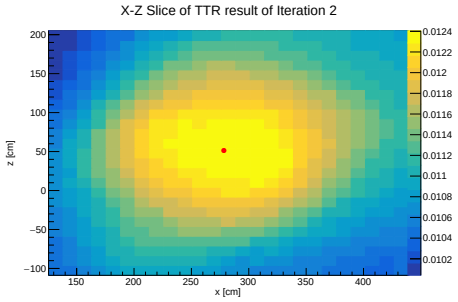

(a) Slice of the X-Z-plane.

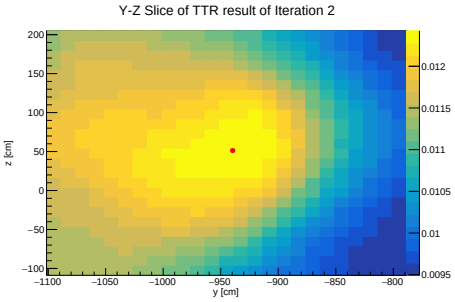

(b) Slice of the X-Y-plane.

Figure A.10: Slices of iteration 2 of erroneous an TTR result for a 1 MeV alpha event. The true vertex is marked with a red dot. (Belongs to Figure 5.10)

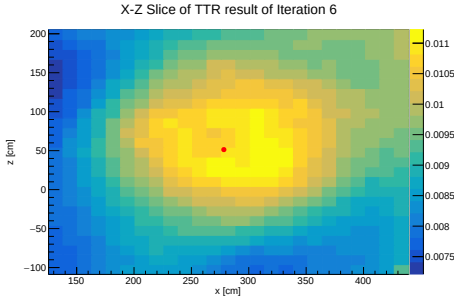

(a) Slice of the X-Z-plane.

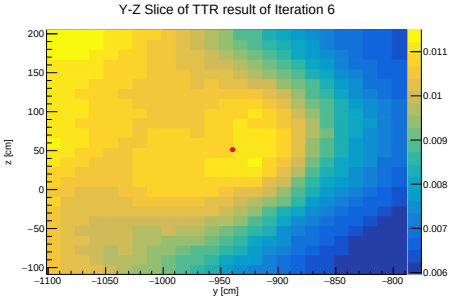

(b) Slice of the X-Y-plane.

Figure A.11: Slices of iteration 6 of erroneous an TTR result for a 1 MeV alpha event. The true vertex is marked with a red dot. (Belongs to Figure 5.10)

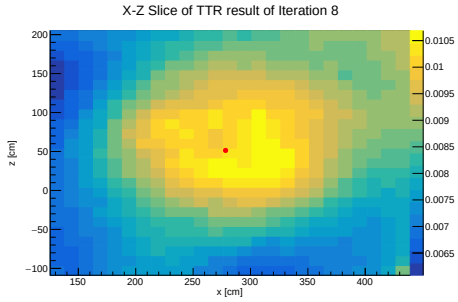

(a) Slice of the X-Z-plane.

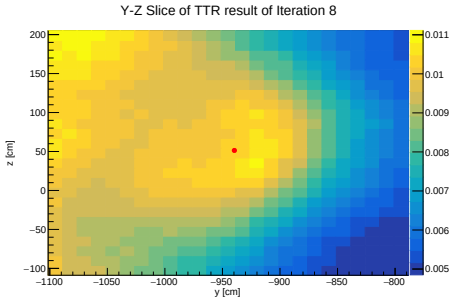

(b) Slice of the X-Y-plane.

Figure A.12: Slices of iteration 8 of erroneous an TTR result for a 1 MeV alpha event. The true vertex is marked with a red dot. (Belongs to Figure 5.10)

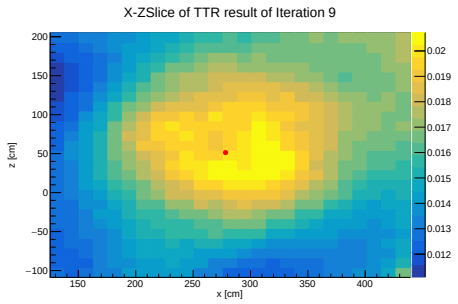

(a) Slice of the X-Z-plane.

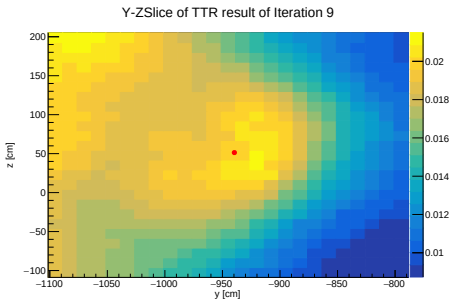

(b) Slice of the X-Y-plane.

Figure A.13: Slices of iteration 9 of erroneous an TTR result for a 1 MeV alpha event. The true vertex is marked with a red dot. (Belongs to Figure 5.10)